TRIBHUVAN UNIVERSITY

INSTITUTE OF ENGINEERING

PULCHOWK CAMPUS

THESIS NO.: M-121-MSTIM-2020-2022

Numerical Analysis on Stall Suppression of a NACA 0012 Airfoil

By

Ashim Chhetri

A THESIS REPORT

SUBMITTED TO DEPARTMENT OF MECHANICAL AND AEROSPACE ENGINEERING IN PARTIAL FULFILLMENT OF THE REQUIREMENT FOR THE DEGREE OF MASTER OF SCIENCE ENGINEERING IN TECHNOLOGY AND INNOVATION MANAGEMENT

DEPARTMENT OF MECHANICAL AND AEROSPACE ENGINEERING

LALITPUR, NEPAL

SEPTEMBER, 2022

COPYRIGHT

TRIBHUVAN UNIVERSITY

INSTITUTE OF ENGINEERING

PULCHOWK CAMPUS

DEPARTMENT OF MECHANICAL AND AEROSPACE ENGINEERING

The undersigned certify that they have read, and recommended to the Institute of Engineering for acceptance, a thesis entitled "**Numerical Analysis on Stall Suppression of A NACA 0012 Airfoil**" submitted by Ashim Chhetri in partial fulfillment of the requirements for the Degree of Master of Science in Technology and Innovation Management.

_____

Supervisor, Sudip Bhattrai, PhD
Asst. Professor, Department of Mechanical and Aerospace Engineering, Pulchowk Campus

_____

External Examiner, Ashish Manandhar
Maintenance Planner, Technical Support Division, Buddha Air

_____

Committee Chairperson, Surya Prasad Adhikari, PhD
Head, Department of Mechanical and Aerospace Engineering, Pulchowk Campus

Date: September 15, 2022

ABSTRACT

Stall suppression is vital during takeoff, maneuver, and landing. It becomes more crucial when the flow is at low Reynolds number as the separation of bubbles is commonly encountered. There are active and passive methods to control such separation and delay stall. For the present study burst control plates (BCPs) is used on upper surface of airfoil, which is a passive method. Two-dimensional symmetrical (National Advisory Committee for Aeronautics) NACA 0012 airfoil of chord (c) length 200 mm is numerically analyzed using ANSYS FLUENT at low Reynolds numbers of 1.3×10^5 with and without burst control plates for determine the aerodynamic characteristics. Initially mesh independence study is done at 8^o angle of attack for different number of mesh elements. 408,400 number of mesh element is selected for further study. Transition SST model is used for numerical simulation studies of airfoil with BCPs as coefficient of lift agree very well with experimental data.

The main objective of this thesis is to improve performance of airfoil at low Reynolds number by suppressing stall using rectangular cross-section BCP and find the optimum size and optimum location. Here, rectangular cross-section BCPs of a constant height 0.005c and of five different widths (0.008c, 0.016c, 0.024c, 0.032c and 0.040c) are numerically analyzed at four different positions (0.045c, 0.05c, 0.07c and 0.1c) from airfoil leading edge using ANSYS FLUENT software with transition SST model. Coefficient of lift (C_L), coefficient of drag (C_D), and coefficient of pressure (C_P) are studied at different angles of attack (α) for various configurations. BCPs of thickness 0.032c and 0.040c located at 0.045c and 0.05c, suppressed stall by 4°. Other configurations suppressed stall by 2°. Stall suppression by BCP at 0.045c of a thickness 0.032c is found to be the most effective among various configurations.

ACKNOWLEDGEMENTS

I would like to express my heartfelt gratitude and sincere appreciation towards my thesis supervisor Dr. Sudip Bhattrai, for his professional advice and suggestions throughout the proceedings of the thesis. I would also like to express my sincere appreciation to the Department of Mechanical and Aerospace Engineering and Institute of Engineering for their support to the thesis. My appreciation is extended to Dr. Surya Prasad Adhikari, Head of Department of Mechanical and Aerospace Engineering, Pulchowk Campus for his co-operation and guidance. I would like to express my sincere gratitude and thanks to Dr. Sanjeev Maharjan, program Co-ordinator, MSTIM for creating an excellent interactive atmosphere for thesis work. I appreciate the suggestion, information, assistance and productive criticism from colleagues and teachers. Finally, I cannot stay without expressing my sincere gratitude and thankfulness to my family members for their encouragement and continual source of inspiration during the entire period of this thesis work. I would also want to express my gratitude to all my 076MSTIM colleagues and MSc. Hostel companions for their unwavering ideas and suggestions.

Inadvertently if any inclusion for the gratitude is forgotten, I would like to express my sincere gratitude to all those who have directly or indirectly assisted me with my thesis work.

TABLE OF CONTENTS

LIST OF FIGURES

LIST OF TABLES

LIST OF SYMBOLS

a	Lift curve slope for a finite wing
a_0	Lift curve slope for an airfoil
c	Chord length
c_f	Skin friction coefficient
C_D	Drag coefficient of an airfoil
C_L	Lift coefficient of an airfoil
C_P	Pressure coefficient
A	Axial force
N	Normal force
D	Drag
L	Lift
h	Height of the rectangular cross-section burst control plate
w	Width of the rectangular cross-section burst control plate
p	Pressure
q_∞	Dynamic pressure
R_e	Reynolds number
V	Velocity
V_∞	Freestream velocity
y	Wall distance
y^+	Non-dimensional wall distance
α	Angle of attack
δ	Boundary layer thickness
μ	Dynamic Viscosity
v	Kinematic Viscosity
ρ	Air Density

τ	Shear Stress
τ_{∞}	Wall shear stress

LIST OF ACRONYMS AND ABBREVIATIONS

2D	Two-Dimensional
3D	Three-Dimensional
BLT	Boundary Layer Trip
BCP	Burst Control Plate
CFD	Computational Fluid Dynamics
DES	Detached Eddy Simulation
DNS	Direct Numerical Simulation
LES	Large Eddy Simulation
LSB	Laminar Separation Bubble
NACA	National Advisory Committee for Aeronautics
RANS	Reynolds-Averaged Navier-Stokes
SIMPLE	Semi Implicit Method for Pressure-Linked Equations
SJs	Synthetic Jets
VGs	Vortex Generators

CHAPTER ONE: INTRODUCTION

1.1 Introduction

The most useful structure in the field of aerodynamics and hydrodynamics is the airfoil which has a streamlined curved design that when in relative motion with surrounding fluid generates a useful reaction force called lift and also generate drag force opposing its motion. It has a variety of applications especially in the field of transportation (airways, waterways) as wings, flaps, rudders, stabilizers, fins, rotor blades, ailerons, etc. have airfoil structures. Wind turbine blades, and water turbine blades have an airfoil shape structure for extracting energy from flowing fluid. The main purpose of an airfoil is to generate lift. Lift coefficient and drag coefficient of an airfoil mainly depends upon the relative motion between fluid and airfoil. High-velocity fluid generates high lift as well as high drag. The important parameter to define velocity of flowing fluid is Reynolds number (Re). It is the ratio of inertia force to viscous force. High-velocity fluid has high inertia force and viscous force is less resulting high Reynolds number. A flowing fluid of a high Reynolds number has high inertia, and the flow is called turbulent. A fluid flow that has viscous force more dominant than inertia force has laminar flow. Flow at less Reynolds number has less coefficient of lift and a high coefficient of drag as laminar flow is thick and fragile. Reynolds number of less than 5×10^5 is considered to be low (Shah et al., 2012). So, it is a challenge to obtain high lift and less drag at a low Reynolds number. (Giguere and Selig, 1997). The case of low Reynolds numbers flows occurs on airfoil of planes wing, rudder, stabilizer, flaps, etc. during takeoff and landing, wind turbines blades, sailplanes, unmanned and micro aerial vehicles, etc. A Low Reynolds number indicates higher viscous force over inertia force and viscosity is main cause of boundary layer instabilities resulting in separation of smooth boundary layer (Patrick, 2011) and separation of flow leads to loss of lift coefficient.

The wing of airplane plays a major role in airplane performance during takeoff, cruising, maneuvering and landing. The length of runway, payload capacity, speed, climb rate, etc. have direct or indirect influence of airfoil shape structure in airplane. The two major outcomes of airplane airfoil application are lift and drag. Since from first successful flight, human researchers have tried to decrease drag and improve lift by design optimization of airfoil. One major problem for airplane airfoils is flow separation resulting from low speed of airplane or due to high angle of attack, limiting

the operating performance of airplane. Flow separation causes fall of lift limiting payload and maneuverability. Increase in drag resulting from flow separation causes more fuel consumption. Hence both increase in drag and decrease in lift due to flow separation leads to loss of control of airplane keeping the lives and property in danger.

Flow separation in airfoil airplane wings occur at leading and trailing edge of airfoil. The leading-edge separation of flow on the airfoil upper surface is also known as laminar separation bubbles (LSB) that forms at high angle of attack and low Reynolds number of flow. Low velocity, surface roughness, structure of airfoil, turbulence intensity, etc. also effects LSB. During low Reynolds number the flow over airfoil is laminar possessing low kinetic energy and remains attach to the airfoil surface. When pressure reverses on the upper surface of airfoil, air flowing from low pressure to high pressure towards trailing edge (called adverse pressure gradient), there is adverse loss of kinetic energy of flow resulting in separation of flow from airfoil. As flow separates it mix-up energy with upper layer of flow becoming turbulent shear layer flow. As the turbulent shear layer flow possess sufficient energy to overcome the negative pressure gradient, the layer again reattaches forming a small bubble. The small zone of recirculating air between the separation of laminar layer and reattachment of turbulent shear layer is called as laminar separation bubble (LSB). LSB can be short or long. Long LSB are formed when velocity of flow decreases or when angle of attack of airfoil increases. The phase of bubble formation is: formation of short bubble, short bubble burst and formation of long bubble. Short bubble burst as angle of attack is increased beyond limit, and stall occurs due to sudden decrease of lift on airfoil. During short bubble burst, the separated laminar flow do not gain enough energy to reattach. Proper control of bubble burst or increasing the limit for a bubble to burst can result a significant improvement in the lift and drag characteristics of an airfoil. The highest negative pressure coefficient indicates formation of short bubble with high slope of reattachment. As angle of attack increase, the negative pressure coefficient decreases forming a small flat slope for reattachment indicating formation of long bubble. The short bubble and long bubble indication can be seen from pressure coefficient distribution of figure 1.1.

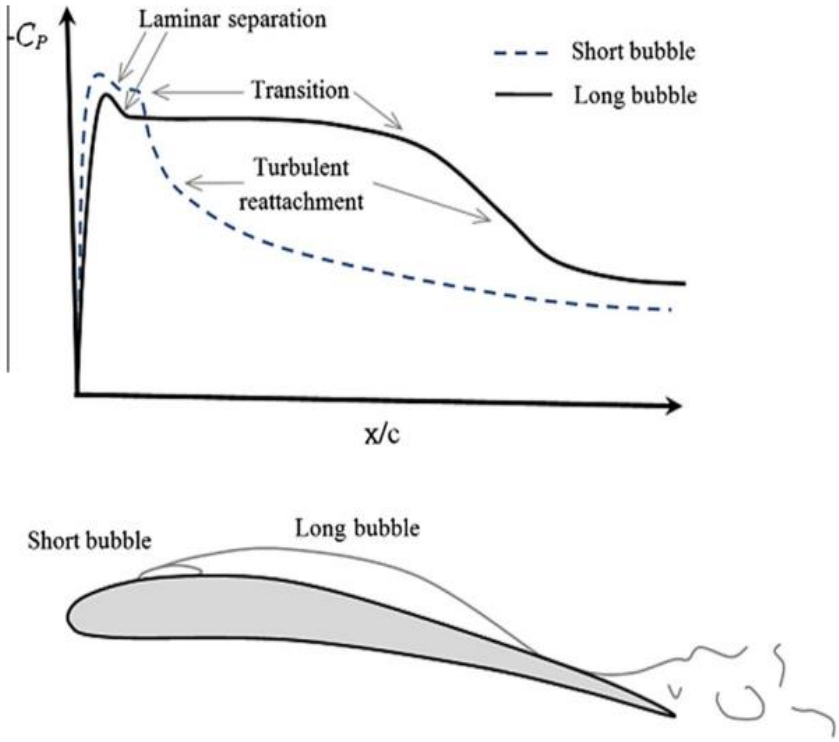

Figure 1.1: Distribution of pressure coefficient due to laminar separation bubble (Choudhry et al., 2015).

The major impact of short bubble is on drag than lift. Smaller the bubble higher the reduction in drag as the thick turbulent boundary layer is reduced. Thinner boundary turbulent layer can be done by reducing separation bubble to increase the airfoil performance. In field of aeronautics engineering the control of flow separation has been a major topic in past decades. Aircraft can take off and land at low speed and smaller runways optimizing the space to take off and land with less risk of fatal accident, when flow separation is controlled.

Flow control means controlling the nature of flow to acquire the desired state (laminar and smoother). Flow control around airfoil is done to avoid flow separation that is essential to decrease drag and increase lift. Flow separation around airfoil occurs mainly on trailing edge and leading edge. There are number of techniques to control flow at leading and trailing edge. Techniques to control flow at trailing edge are active and passive control techniques (Gad-el-hak et al., 1998).

Passive control techniques do not use external energy but active control techniques require external source to operate. Passive control devices are generally geometrical modifications attached on airfoil to divert flow direction. These devices are simple,

cheap and don't require electronic components to operate. They operate in subsonic and transonic ranges of flow. For example: leading edge slat, vortex generator, etc. Vortex generators (VGs) are quite popular in passive devices for flow separation control. They are thin plates usually of triangular or rectangular shape inclined at a certain angle and attach at the upper part of the airfoil. They have a height of boundary layer of flow and create vortices mixing low energy bottom layer of flow to high energy upper layer of flow. These re-energies the flow to work against adverse pressure gradient to remain attached on the surface of the airfoil increasing lift and decreasing drag. Vortex generators are small vanes attached on the wing's suction surface and blades of turbomachines in geometric patterns. One of the major drawbacks of vortex generator and other passive control devices are they induce a lot of drag force resulting in a lot of energy loss during operation.

Active control devices use external input energy to control flow separation making it complex but efficient. These devices take less input and result high output effect. Controlling of dynamic process that is complex is easily done through active control devices. For example: a boundary layer jet blowing, oscillatory actuators, plasma actuators, etc. Jet blowing is the injection of high momentum fluid flow into the wall of airfoil energizing the flow layer near wall. Similarly, to jet blowing there is a suction method where the separated flow is sucked back to the boundary layer keeping the fluid flow attach to the airfoil. Both of these are complex system that requires either a compression system or a vacuum system increasing the gross weight of aircraft, which means more fuel consumption. Another active device is Synthetic jets (SJs). The periodic disturbance is produced with this technique by periodic vibration with net mass flux zero going through an aperture, which is brought about by a diaphragm's movement. The separation flow is delayed or lessened as a result of the diaphragm's movement because it creates suction movement and blowing movement due to which flow entrain into the boundary layer close to the surface from outside boundary layer. But in order for the synthetic jet actuator to operate, the optimization method must maximize its flow control effectiveness condition.

Besides the techniques of flow control separation on the trailing edge, there are a few ways to control flow separation on the leading edge of an airfoil. For example: devices such as transition ramps, boundary layer trips, pneumatic turbulators, burst control plates, etc. Burst control plates (BCP) or boundary layer trips (BLT) are passive control

devices. They are simple and present at the leading edge of an airfoil. So, the size and its location are vital for its performance to control flow separation at the leading edge of an airfoil. They are especially useful at low Reynolds number flow, when the drag is increased by laminar separation bubbles. The Tollmien-Schlichting waves become more unstable when BCPs or BLTS are used, which causes turbulent flow. Due to its change from a laminar to a turbulent flow, the transition results in the split and laminar boundary layer reattach. Additionally, by reducing the size of the laminar separation bubbles, pressure drag is decreased.

Among various method of passive flow control technique to control flow separation at leading edge of airfoil, burst control plate is selected for this research study. A rectangular burst control plate is placed on upper part of NACA 0012 airfoil and various sizes of BCPs at various location on airfoil are numerically analyzed by computational fluid dynamics tools. Coefficient of lift, coefficient of drag and coefficient of pressure are compared and analyzed at a low Reynolds number of 1.3×10^5 using software ANSYS FLUENT 2020 R2.

1.2 Problem Statement

Flow separation is one of the major issues in airfoil resulting in the performance limit of airfoil. This limitation increases when flow is considered to be at low Reynolds number because the flow gets quickly detach from airfoil surface. Airfoil at low speed are widely seen in wind turbines, gliders, unmanned aerial vehicles, etc. Controlling of this flow separation is highly beneficial. Leading edge flow separation is common in most airfoil and most effective technique to control flow separation at leading edge is use of burst control plate. The main goal is to reduce the bubble size formed at leading edge. And burst control plate disturb the flow and transfer high energy from upper flow layer to lower flow layer. Researchers have done many numerical and experimental analysis of burst control plates but still the best and efficient way is still in research, as various airfoil may require various configurations.

So, for the present study NACA 0012 airfoil is numerically analyzed at low Reynolds number of 1.3×10^5 with and without rectangular burst control plates to study the lift coefficient, drag coefficient and pressure coefficient at different angle of attacks.

1.3 Objectives of the Study

1.3.1 General Objective

The main objective of this thesis is to enhance the performance of the NACA 0012 airfoil by suppressing the stall at a low Reynolds number of 1.3×10^5 with the attachment of rectangular cross-section burst control plates on the airfoil.

1.3.2 Specific Objectives

- To investigate the effects of plate widths and locations on the stall angle of an airfoil.
- To determine the optimum size and optimum location of the rectangular cross-section burst control plates.

CHAPTER TWO: LITERATURE REVIEW

2.1 Aerodynamic Forces and Moments

There are only two fundamental sources from which the aerodynamic moments and forces on bodies submerged in the fluid are produced: shear stress distribution and pressure distribution over the surface of the body. To the surface, pressure behaves normally. Shear stress acts tangential to the surface and is brought on by air and body friction. The resultant of force and the resultant of moment on the body are caused by the interaction of shear stress (τ) and pressure (P). The components of the resulting force are depicted in figure 2.1. Relative wind, or U_∞, is the speed of the flow far in front of the body. It also goes by the name "free stream velocity." The linear distance between the body's leading and trailing edge is known as the chord "c".

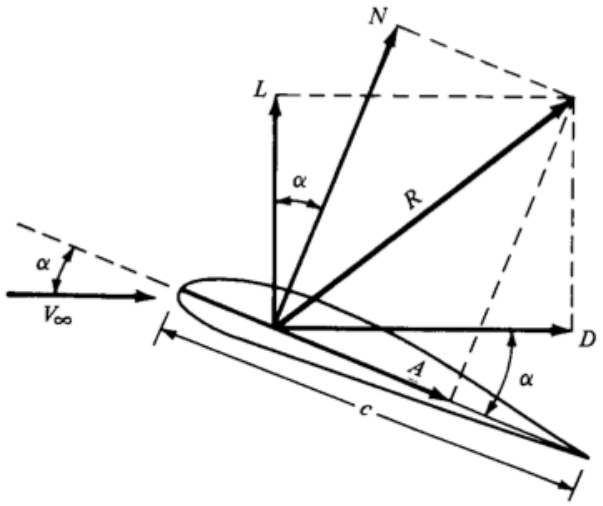

Figure 2.1: Components of resultant aerodynamic force (Anderson, 2007)

By definition,

R = Resultant force

Lift (L) = R component perpendicular to V_∞

Drag (D) = R component parallel to V_∞

Normal force (N) = R component perpendicular to chord (c)

Axial force (A) = R component parallel to chord (c)

Angle of attack (α) = Angle between A and D, or V_∞ and c, or N and L

By using equations 2.1 and 2.2 , it is possible to derive the lift and drag forces from the normal force and axial force.

$$L = N\cos\alpha - A\sin\alpha \quad (2.1)$$

$$D = N\sin\alpha + A\cos\alpha \quad (2.2)$$

In order to measure the lift and drag forces acting on an object, coefficients are used. The wind speed, frontal area, fluid density, and the force an object experiences as a result of fluid flow, all affect these coefficients. To compare aerodynamic properties of bodies, dimensionless lift and drag coefficients are used and defined as in equations 2.3 and 2.4.

$$\text{Lift Coefficient: } C_L = \frac{L}{q_\infty S} \quad (2.3)$$

$$\text{Drag Coefficient: } C_D = \frac{D}{q_\infty S} \quad (2.4)$$

Where "s" represents reference area and dynamic pressure (q_∞) is calculated using equation 2.5.

$$q_\infty = \frac{1}{2}\rho u^2 \quad (2.5)$$

Two-dimensional (2D) airfoil is considered as infinite wing and has different aerodynamic properties when compared to finite three dimensional (3D) wing. The flow around the wing tips of a 3D wing is driven from the high-pressure zone beneath the tips to the low-pressure region on top by the pressure differential between the upper and lower surfaces.

As a result, on the top surface of the wing, there is a span wise flow from the tip toward the wing root, but on the bottom surface, there is a span wise flow from the root toward the wing tip. These flow at wing tips are called wing tip vortices. The small downward component of air velocity caused by the wing-tip vortices downstream of the wing called downwash. In addition to reducing the angle of attack, this downwash create induced drag as the vector of lift force which is tilted backward, as shown in figure 2.2. As a result, the lift coefficient and drag coefficient of infinite airfoil section are different when compared to the coefficient of lift and coefficient of drag of the finite wing at same conditions. This causes an increase in drag coefficient and a decrease in lift coefficient.

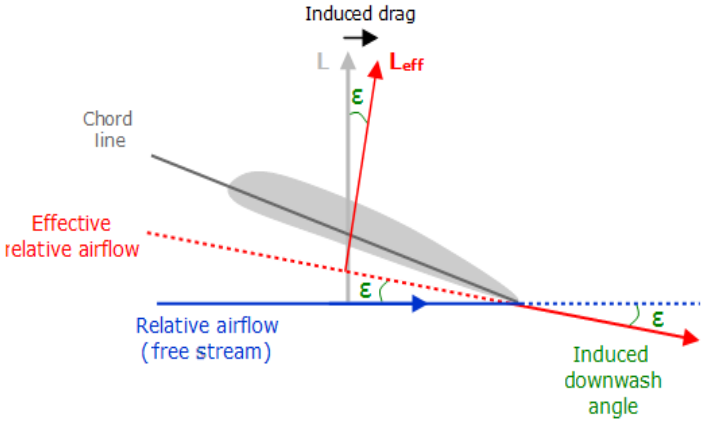

Figure 2.2: Components of generated lift and drag (Anderson, 2007)

2.2 Flow Separation

Figure 2.3 depicts the normal variation of coefficient of lift with angle of attack for an airfoil. Between small and medium angles of attack, the coefficient of lift varies linearly, and the flow remains connected over the majority of the airfoil surface. However, when the angle of attack increases, the flow on the upper surface of airfoil tends to detach, leaving a significant wake behind it, as depicted in figure 2.3 above. Because of the strong viscous effects, this separated flow has far more drag than lift. This state is referred to as stopped and causes a loss of lift, an increase in drag, the production of aerodynamic noise, and the beginning of buffeting. To prevent or postpone the stall, numerous strategies are being developed to enhance the flow around the airfoil. These include synthetic jets, burst control plates, boundary layer trips, and vortex generators. The description of the phenomena is provided to understand the separation of flow physics.

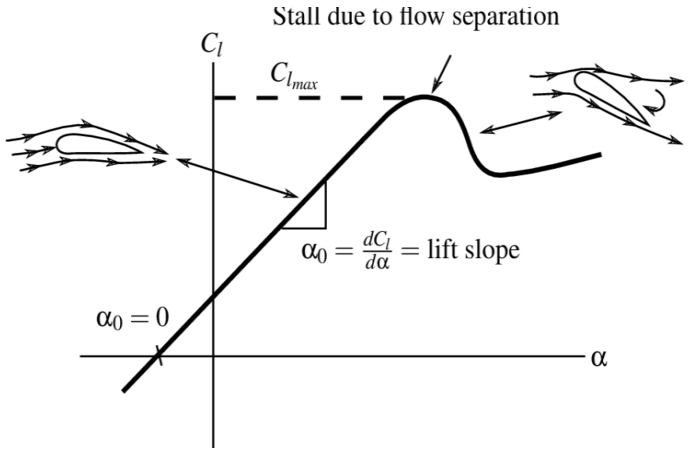

Figure 2.3: Variation of lift coefficient with angle of attack for an airfoil (Anderson, 2007)

A thin zone near the wall where viscosity is present exists for a particular Reynolds number of fluid flow. The boundary layer is that region and depending on how it behaves, it can cause the flow to divide. Boundary layer development may be caused by pressure dispersion across the surface of the airfoil. The boundary layer will adhere to the surface if there is a decrease in pressure along the downstream of flow. The boundary layer may separate, if there is increase in pressure along the downstream of flow due to negative pressure gradient. According to Prandil, if the negative pressure gradient is serve enough, a recirculating fluid flow region or dead region is created due to the backward motion (toward upstream direction) of fluid particles near the surface and flow separation occurs. This is because the fluid particles kinetic energy inside the layer decrease closing to the wall to zero, when the velocity decreases closing to the wall in the boundary layer.

The velocity outside the boundary layer varies as the flow occurs around airfoils and curved surfaces. From Bernoulli's equation, it may be inferred that pressure rises when velocity falls and vice versa. The pressure gradient is known as “adverse pressure gradient”, when the velocity is decreasing, or when dp/dx is positive. Negative dp/dx is referred to as "favorable gradient of pressure”. Figure 2.4 shows the boundary layer velocity profile development of a flow over the wall in an area having an adverse pressure gradient. Upstream of the point of separation, the velocity gradient $\frac{du}{dy}$ is positive; however, at the point where the flow separates it is zero and when the fluid flow direction is in reverse, it turns negative. The shear layer may produce a wake and not reattach to the wall surface or it may reattach to the wall surface.

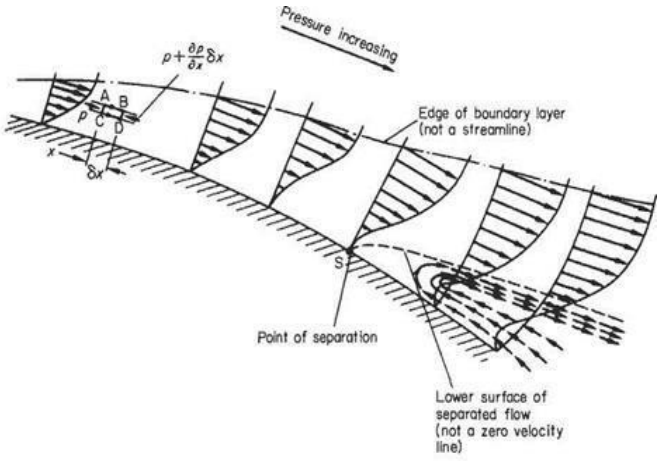

Figure 2.4: Flow before and after the point of separation in boundary layer (Anderson, 2007)

2.3 Laminar Separation Bubble

Laminar separation bubbles have a significant impact on a performance of aircraft at small Reynolds numbers. A significant negative pressure gradient causes to split the boundary layer that is laminar from the curved surface of airfoil, which results in a separation bubble formation. As a result of disturbances, the separated laminar flow eventually transforms into a turbulent flow. The outside limit of the separated flow area is where the transition region (which is not quite a point of transition) is situated, away from the airfoil. The airfoil surface may once more be reached by a turbulent wedge as the turbulent boundary layer thickens quickly. The reattachment point is the location where the turbulent flow once more touches the surface. A laminar separation bubble is an area that is bounded by areas of separated laminar flow and turbulent flow. There may be a circulation of the flow inside the bubble. It's possible that the flow direction close to the airfoil surface will be the exact opposite of the outer flow. The laminar separation bubble is remarkably stable due to the virtually complete lack of energy exchange with the outside flow. The boundary layer becomes thicker due to the separation bubble, which increases airfoil drag. Without a separating bubble, the increase in drag can be many times more than the airfoil drag. The growth of laminar separation bubbles also affects lift and moment, which can cause issues with a model aircraft's stability and control.

An LSB schematic is shown in figure 2.5. Normally, the boundary layer is laminar at first, but when it comes into contact with an unfavorable pressure gradient, it separates. Due to its instability, the laminar separated shear flow transforms into a turbulent separated shear flow. The stream transfer the momentum that is free to the surface below by passing through the shear layer due to turbulence. When transport of momentum is adequate, the turbulent boundary layer rejoins the surface sealing the separating bubble.

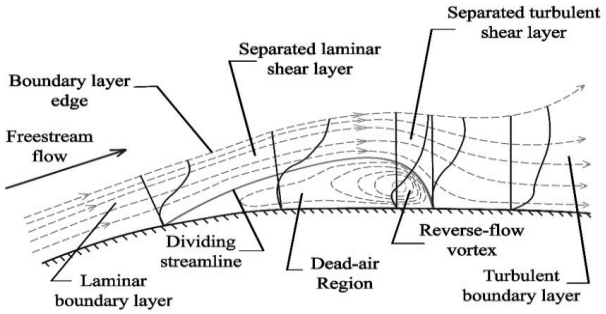

Figure 2.5: Details of a laminar separation bubble

2.4 Flow Separation Control

Although potential flow theory addresses a number of fluid mechanics phenomena, most boundary layer situations, like the flow field surrounding an airfoil, cannot be adequately explained by it. The boundary layer will keep growing as long as there is no pressure difference along the hard surface. When there is negative pressure, the boundary layer's thickness dramatically increases. The negative pressure and shear (viscous) forces that reduce boundary layer momentum prevent the boundary layer from expanding along a considerable length of surface also called as separation. Significant energy losses and limitations on an aircraft's ability to fly aerodynamically are caused by the boundary layer separation. Therefore, one of the main challenges facing aerodynamicists today is controlling the boundary layer. If separation across an airfoil can be prevented, the boundary layer will remain thin, the pressure drop at the trailing edge will not occur, and as a result, the drag force will drop to its lowest possible level (Schlichting, 1968).

In order to improve the performance of aerodynamic bodies, a variety of flow control techniques are either applied experimentally or computationally to govern flow around the body. These can lessen drag, increase lift and increase stall angle in the case of aircraft wings, by postponing flow separation. Since the presence of the boundary layer produces numerous design and engineering issues, particularly in the field of aerodynamics, a considerable number of researches have recently concentrated on the impacts of the boundary layer on the lift and drag forces. Boundary layer separation control, also known as flow separation control, is a term used to describe methods created for manipulating boundary layers. The primary objective of boundary layer control over an airfoil is to postpone separated flow, which increases lift and decreases drag force. This improves airfoil performance by raising the lift-to-drag ratio and postponing stalls. Additionally, they offer flow-induced noise reduction and mixing augmentation (Gad-el-hak et al., 1998).

The primary criterion for categorizing various flow control strategies is whether they are active or passive. There are two ways to manage flow separation: passively, which doesn't require a controller; and actively, which does need a controller and controlling sensors to gather data on the flow field. Passive methods have no energy expenditure; the flow field is changed by deflecting the control surfaces, such as flaps and ailerons, or by fixed geometric devices. Active control employs energetic forcing flow control

techniques. These techniques call for additional energy input and a control device that allows the flow control to be activated and deactivated. Active methods can therefore only be utilized when necessary and won't result in extra losses when they aren't, as at high Reynolds numbers. Depending on the local flow state, it can have a different input power level. Other benefits of active flow management include the capacity to influence complex dynamical processes, such as the reduction of skin friction and therefore viscous drag in turbulent boundary layers, and the ability to achieve a significant effect with tiny, localized energy input. The active flow control can be separated into two categories: predefined and reactive, as schematically seen in figure 2.6. Regardless of the flow state, predetermined active flow control, also known as open loop control, involves both uniform and uneven energy expenditure. Reactive flow control is a specific type of active flow control where the power consumption of the controllers is continuously adjusted by parameters obtained from on-site sensors where the control loop can be either closed feedback or open feed-forward (Gad-el-hak, 2000).

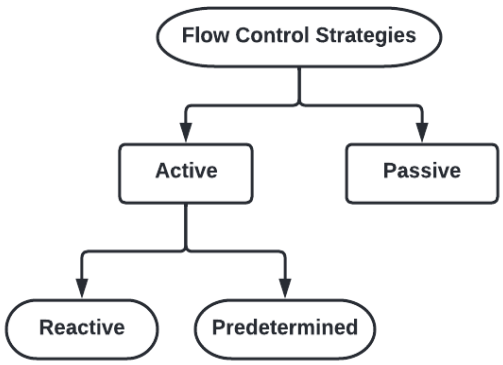

Figure 2.6: Techniques of flow control

There are several different devices that are used for the passive flow control technique, including vortex generators, serrated trailing edges, distributed roughness, streamlining, and uniform blowing and suction. On the other side, some active flow control techniques include heating a wall, moving surface elements (such as trailing edge flaps), oscillatory blowing and suction, air jet vortex generators, and artificial jets. Some high-lift systems have the ability to passively adjust the flow by blowing air through trailing-edge flaps and leading-edge slats. Air from the wing lower surface travels across the upper portion of wing as the high energy fluid is injected to increase the energy of the boundary layer during the deployment of the high-lift systems. Despite the fact that the efficiency of the devices may be limited by the difference in pressure

between the lower and upper surfaces, this technique may drastically alter the body's drag and lift (Abbott and Von Doenhoff, 1959).

Flaps and ailerons, two examples of control surfaces on a transport aircraft, increase both lift and drag. The majority of these control surfaces regulate the flow over airfoils using passive techniques of flow control. Due to separation of flow, at greater angle of attack the efficiency of the control surfaces decrease; however, this issue can be solved by using a flow control approach. This strategy allows for flow management while maintaining aerodynamic effectiveness.

2.5 Computational Fluid Dynamics

In order to evaluate and address issues relating to fluid flow, computational fluid dynamics (CFD), a branch of fluid mechanics, uses mathematical relationships and algorithms. The demand for quicker and more precise ways to compute the flow fields surrounding technical interest setups has fueled the rapid development of CFD. CFD was the method of choice in the previous few decades for the design of many industrial, automotive, and aerospace parts and processes where fluid or gas flows are important. There are numerous commercial CFD packages for modeling flow in or around objects that are accessible in fluid dynamics. The features and intricacies displayed by the computer models are either impractical, prohibitively expensive, or both to quantify or see experimentally.

Making the geometry and meshes with a preprocessor is the initial step in problem modeling. In the industry, properly producing a mesh for the domain geometry that enables a trade-off between desired accuracy and solution cost typically takes up the majority of time spent on a CFD project. A solver can solve the problem's governing equations once the mesh has been created. The following are the fundamental measures that must be taken in order to solve the issue. Prior to creating the model geometry and mesh, the modeling objectives must be established. The solution is then computed and monitored using the solver and the physical models at a higher level. The results are then analyzed, recorded, and, if necessary, changes to the numerical or physical model parameters are taken into consideration. (Ferziger and Peric, 1996)

2.5.1 Turbulence Modeling

To develop Reynolds Averaged Navier-Stokes equations, turbulence models typically attempt to change the original unstable Navier-Stokes equations by adding averaged

and fluctuating quantities (RANS). Because of the statistical mean method used to get the equations, the turbulence models based on the RANS equations are known as statistical turbulence models.

RANS is a method of turbulence modeling that is most frequently used in Computational Fluid Dynamics (CFD). The instantaneous Navier-Stokes equations' solution variables are divided into mean and fluctuating components in this method. Velocity for a turbulent flow u_i, is considered equal to sum of the mean velocity component $\underline{u_i}$ and the fluctuating velocity component u_i' as shown in the equation 2.6.

$$u_i = \underline{u_i} + u_i' \tag{2.6}$$

The continuity and momentum equations that incorporate mean velocity component ($\underline{u_i}$) and fluctuating velocity component (u_i') are shown in equation 2.7 and 2.8.

$$\frac{\partial \rho}{\partial t} + \frac{\partial (\rho u_i)}{\partial X_i} = 0 \tag{2.7}$$

$$\frac{\partial (\rho u_i)}{\partial t} + \frac{\partial (\rho u_i u_j)}{\partial x_i} = \frac{\partial \rho}{\partial x_i} + \frac{\partial}{\partial x_j}\left[\mu\left(\frac{\partial u_i}{\partial x_j} + \frac{\partial u_j}{\partial x_i} - \frac{2}{3}\delta_{ij}\frac{\partial u_i}{\partial x_i}\right)\right] + \frac{\partial}{\partial x_i}(-\rho\underline{u_i' u_j'}) \tag{2.8}$$

The above set of equations represented in Cartesian coordinates are the RANS equations, with ensemble-averaged (or time-averaged) solution variables, and the additional Reynolds stress terms $-\rho\underline{u_i' u_j'}$, are modeled using various turbulence models.

The Reynolds stress and mean velocity are related using Boussinesq hypothesis as shown in equation 2.9.

$$\left(-\rho\underline{u_i' u_j'}\right) = \mu_t\left(\frac{\partial u_i}{\partial x_j} + \frac{\partial u_j}{\partial x_i}\right) - \frac{2}{3}\left(\rho k + \frac{\mu_t \partial u_k}{\partial x_k}\right)\delta_{ij} \tag{2.9}$$

1. Transition SST Model

This turbulence model is applied in simulating transitional flows. k-ω SST model is capable of simulating such flows since it solves additional two equations for intermittency γ and transition onset Reynolds number ($Re_{\theta t}$) along with continuity and momentum equation. Onset of intermittency is indicated by the critical Reynolds number ($Re_{\theta c}$). $P_{\gamma 1}$ and $E_{\gamma 1}$ are the transition sources whereas $P_{\gamma 2}$ and $E_{\gamma 2}$ are the destruction sources.

γ is transported throughout the flow-field governed by the equation 2.10.

$$\frac{\partial \rho\gamma}{\partial t} + \frac{\partial \rho U_j \gamma}{\partial x_j} = P_{\gamma 1} - E_{\gamma 1} + P_{\gamma 2} - E_{\gamma 2} + \frac{\partial}{\partial x_j}\left[\left(\mu + \frac{\mu_t}{\sigma_\gamma}\right)\frac{\partial \gamma}{\partial x_j}\right] \quad 2.10$$

And equation 2.11 shows the transport equation for $Re_{\theta t}$.

$$\frac{\partial \left(\rho \underline{Re_{\theta t}}\right)}{\partial t} + \frac{\partial \left(\rho U_j \underline{Re_{\theta t}}\right)}{\partial x_j} = P_{\theta t} + \frac{\partial}{\partial x_j}\left[\sigma_{\theta t}(\mu + \mu_t)\frac{\partial \underline{Re_{\theta t}}}{\partial x_j}\right] \quad 2.11$$

The k-ω SST equation is modified and coupled with the transition model as shown in equation 2.12.

$$\frac{\partial}{\partial t}(\rho k) + \frac{\partial}{\partial x_j}\left(\rho k u_j\right) = \frac{\partial}{\partial x_j}\left((\mu + \sigma_k \mu_t)\frac{\partial k}{\partial x_j}\right) + P_k^* - D_k^* \quad 2.12$$

Where, P_k^* denotes production term for the original SST model given by equation 2.13 and D_k^* denotes destruction term for the original SST model given by equation 2.14.

$$P_k^* = \gamma_{eff} P_k \quad 2.13$$

$$D_k^* = min\left(max\left(\gamma_{eff}, 0.1\right), 1.0\right) D_k \quad 2.14$$

y^+ value is a crucial factor to be considered in capturing laminar and transitional flow behavior. $y^+ \leq 1$ must be satisfied to resolve the viscous sub-layer. In case of large y^+ values ($y^+ > 5$), with increasing y^+, the transition onset location relocates to upstream of the flow.

2.6 Related Works

In 1904, Prandtl conducted first study on flow separation control techniques. A cylindrical surface is subjected to boundary layer suction technique to delay separation of boundary layer. In order to control the boundary layer and postpone flow separation, he applied a blowing jet around a circular cylinder, as seen in some experimental data. He then described the physics underlying flow separation. In late 1930s and 1940s first known experiment of boundary layer suction technique was conducted on wings (Richards & Burge, 1943: Braslow, 1999: Kitsios, et al., 2006).

Performance of airfoil is bad for Reynolds numbers less than 70,000, according to Lissaman (1983). The performance of airfoil can be improved by using various devices through fast transitions, if Reynolds numbers ranges from 70,000 to 500,000. The

boundary layer is energized throughout this phase, which keeps the flow from separating. Synthetic jets, vortex generators, surface blowing or suction, boundary layer trips (rod, grit, tube, wires, or tape strips), and many other devices can be used. Even though boundary layer trips can cause some losses and may not improve performance, it may be still useful to study about them to understand the flow nature.

In several studies, the passive flow control has been a topic of attention. Vortex generators (VGs) are a well-known traditional passive control method that was developed in the 1940s. The VGs are typically positioned at the local velocity vector incidence and are composed of a collection of tiny trapezoidal, triangular, or rectangular vanes that are roughly height of boundary layer. Depending on how they are configured, the VGs can produce a cluster of vortices that are rotating in opposite direction or a pair of vortices rotating in same direction. The created vortices increase the boundary layer's resistance to separation by entraining greater velocity fluid from the boundary layer's outer region to the near-wall region. The VGs' benefits are their light weight, durability, affordability, and simplicity. But conventional VGs with heights equivalent to the eight times of thickness of boundary layer significantly increase parasitic drag. They efficiently control flow separation. Reducing the VGs height from the magnitude of 8 to 0.28 or less is one way to enhance their performance. Micro VGs, sub boundary layer VGs, submerged VGs, and low-profile VGs are all smaller than standard VGs in terms of height. To overcome the flow separation, the micro VGs still generate a variety of small stream wise vortices, with less parasitic drag. However, VGs do have significant drawbacks. They can only be useful over a limited operational range since they lack the capability to deliver a time-varying control action. Furthermore, VGs will always create parasitic drag.

The vortex generators should be put near the natural separation point to postpone the separation. The device height and spacing are significant design criteria in addition to the position of the vortex generator. Although the additional drag is reduced with decreasing vortex generator size, at low Reynolds numbers, a small vortex generator might not be enough to cause reattachment. Lin, 1990 presented a comprehensive analysis of low-profile vortex generators (with a device height ranging from 10% to 50% of the boundary layer thickness). The vane-type generators are the most effective in reducing the separation region, according to his investigation of a variety of low-profile vortex generators. Tay et al. studied dimples and concluded that drag reduction

might be improved by increasing the dimple depth from 1.5% to 5% of its diameter. However, greater dimple depth can lead to increased flow separation, which can cause additional drag. So, with higher Reynolds numbers, deeper dimples are more suited.

Three dimensional trips, repeated two dimensional plain trips and single two dimensional plain trip were three different boundary layer trips studied by Lyon et al. (1997) on the SD7037, E374, and M06-13-128 airfoils at 100,000 to 300,000 range of Reynolds number. Even though the trip height was raised, the overall drag was reduced as a result of the bubble's size being shrunk, which had a more significant impact than raised device drag. The ideal trip heights are said to decrease as the Reynolds number increases. Comparing several two dimensional trips to a single two dimensional trip, it was discovered that at the tested heights of trip, the drag on the three multiple trips was a little bit lower. This suggests that drag of additional device from several trips was balanced by higher disruptions of flow, and lowered bubble drag. All investigations have demonstrated that employing boundary layer trips was most advantageous for airfoils with large laminar separation bubbles. Trip effectiveness results from three interrelated factors, the size of which is airfoil dependent: increased trip device drag, changes in bubble drag (pressure drag), and changes in skin friction drag. When a trip is added to an airfoil with a large bubble, the bubble drag often decreases significantly, which is a significant improvement over the drag increase caused by the trip device drag and additional skin friction drag.

On a NACA 0012 airfoil, Huang et al. (2004) investigated the suction and blowing flow control approaches. As perpendicular suction at the leading edge increased in compared to other suction circumstances, the relationship between jet location and angle of attack revealed a notable variation in lift coefficient. Additionally, it was discovered that the tangential blowing in downstream sites caused the greatest rise in the lift coefficient value.

For the improvement of aerodynamic characteristics and to postpone burst of laminar separation bubble at 130,000 Reynolds numbers, Wong et al. (2009) examined the burst control plate (BCP) effectiveness at various positions (5%, 7.5%, and 10% of chord length of an airfoil) on a NACA 631-012 airfoil. The height, width, and location of the plate's trailing edge serve as the criteria for regulating the burst control's efficacy. According to the experimental findings, increasing the height of plate (h/c) from 5% to 7.5% likewise causes an increase in the airfoil's stall angle for both plates types

(rectangular and thin plates). For each of the examples examined, the maximum coefficient of lift was raised. The plate is advised to be positioned in front of the reattachment point of flow, with the height of leading-edge being equal to the separated shear layer height. For an angle of attack greater than 9°, the drag is substantially reduced and the lift created is significantly more than that of an airfoil with no burst control plate. The overall findings demonstrated that using a burst control plate can be a successful strategy for preventing bubble burst and postponing airfoil stall at low Reynolds numbers.

More and more research on boundary layer control is being done using the CFD approach. The effects of passive flow control devices on the aerodynamic performance of airfoils have been the subject of numerous flow control research using CFD methods. The transition from laminar to turbulent flow is crucial for identifying flow features and evaluating airfoil performance, such as lift and drag, when modelling the flow across airfoils. Therefore, a more accurate drag forecast will undoubtedly result from proper transition modeling that considers both the beginning and extent of transition.

To examine the aerodynamic properties of a wing with a NACA 0012 airfoil section, Kianossh et al. (2015) performed a three-dimensional suction flow control research. The leading edge of the wing was designed with center suction and tip suction, two separate suction slot distributions. According to the findings, both the center suction distribution and the tip suction distribution's lift-to-drag ratios rise with the length of the suction jet. However, the total aerodynamic performance was improved more successfully by the center suction distribution. The researchers concluded that the center suction consistently outperforms the tip suction when the jet length is larger than half the wingspan while the tip suction is more effective when the jet length is less than half the wingspan.

Using the Transition SST model at a 10% Reynolds number, Sreejith et al. (2018) carried out a numerical investigation on the impact of boundary layer trips on the aerodynamic performance of the E216 airfoil. He analyzed the influence of BLT on LSB formation over the airfoil and the performance of the airfoil. He also looked at flow behavior and the impact of angle of attack on LSB formation. Different trip heights (0.3 mm, 0.5 mm, 0.7 mm, and 1 mm) and two distinct trip positions (17% of chord and 10% of chord from leading edge) were examined. The results demonstrated that boundary layer trip might partially or totally remove LSB and enhance the airfoil's

aerodynamic characteristics. At an angle of attack of 6°, the maximum reductions in drag of 15.48% and lift to drag ratio of 21.62% were achieved.

Rinoie et al. (2009) carried out the first investigation on short bubble burst control as a technique of preventing airfoil stall. One of the unique ideas was to intentionally control the formation of the separated shear layer by inserting a thin plate within the short bubble. Their experimental findings showed that the vortices developed at the plate trailing edge increase those created by Kelvin- Helmholtz disturbances within the split shear layer, which drives the divided shear layer to rejoin downstream of the plate. Due to which, the stall angle of NACA 0012 airfoil sections and maximum lift coefficient were also raised. According to Kurita et al. (2008), applying the plate with rectangular cross section to the same airfoil section was more successful than applying a thin plate, further suppressing the leading-edge stall due to the reattachment of circulating flow to the surface of airfoil approaching stall and modifying the characteristics of lift.

Grager, et. al. (2011) study employed a "dynamic burst control plate" that oscillates plate dynamically. They stated that this form of burst control plate efficiently suppresses stalls. Nakamura, et. al. (2012) investigated the effect of leading edge and trailing edge position for burst control plates of rectangular cross-section with width, w/c=0.008 and height, h/c=0.005, for stall suppression, and found the best position with respect to the leading edge of airfoil to be X_P/c=0.050. Another study conducted by Shrestha et al. (2019) investigated the best possible height of BCP for the NACA 0015 airfoil, which is found to be 1mm at 0.2c position for best stall suppression.

CHAPTER THREE: RESEARCH METHODOLOGY

The effect of different configurations of burst control plate (BCP) are numerically studied on NACA 0012 airfoil. First, the input parameters are determined, that are: the changing widths and various installed locations. Width is changed in the range between 0.8% and 4% of chord length with a gap of 0.8% and positions are changed in the range of 4.5% to 10% of chord length as per the previous study and available experimental data for ease of present research. The output results are derived in the form of lift coefficient and drag coefficient for ease in comparison of useful effect. The input parameters are processed to obtain desired output by the use of computational fluid dynamics software ANSYS FLUENT.

Figure 3.1 shows the flowchart of the research methodology applied for this research. Initially, a deep study related to the research topic is searched and noted thoroughly. After collecting all the required information, a physical model resembling the study is created in ANSYS FLUENT design modeler. Then structured mesh of quadrilateral elements surrounding the domain is created using the edge sizing technique in FLUENT. Inflation layer is created near the boundary of airfoil surface and around burst control plate. Boundary conditions are set up resembling the experiment conditions based on previous research. After that simulation or numerical analysis is carried out with a certain number of mesh elements. To find the appropriate mesh element number for saving time and accuracy, mesh independence test is carried out with an increasing number of elements. First a coarse mesh is created by using less number of elements and then elements number are increased making the mesh finer. For all the cases lift coefficient are measured and if the error percent in between cases is less than 1%, then, the obtained mesh element number is selected for further study. Before studying other configurations, the validity of setup is checked by comparing the experimental data and obtained numerically analyzed data. If the error percent in comparison is less than 10% the study is further carried out, otherwise, the setup is rechecked and modified as per the requirement through different turbulence models, etc. After finalizing the mesh element number and setup conditions, the study of different configurations of burst control plates are carried out and obtained results are compared. Finally, the effect of different configurations are analyzed on basis of lift coefficient, drag coefficient and stall angle. At last all the generated results are noted and documented.

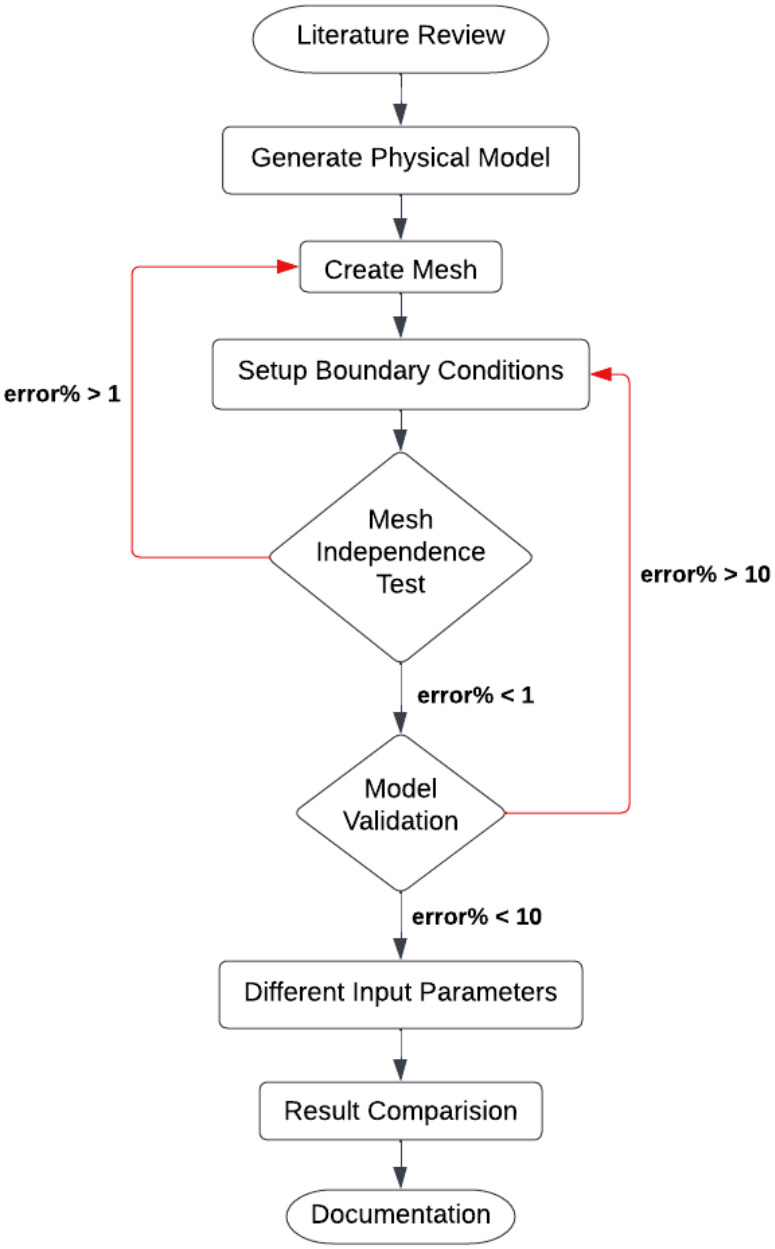

Figure 3.1: Flowchart of research methodology

By numerically resolving 2D RANS equations, the flow field around the airfoil is obtained. As per the numerical analysis carried out by Shrestha, 2019 on NACA 0015 clean airfoil, the Transition SST model was found to be the best model resembling the experimental data. For this study same model is used for the solution of the fluid flow problem.

To evaluate the characteristics of flow near the wall, a 2D analysis of flow using ANSYS FLUENT 2020 R2 was done to examine the lift force and the drag force acting

on the airfoil. The meshes around the airfoil and the flow domain were made using FLUENT 2020. The variation in mesh structure is mostly influenced by the grid points number near to the surface and y^+. The spatial resolution of the mesh close to the wall (y^+) surrounding the airfoil must be fine enough to capture the characteristics of flow for the turbulent flow analysis. In order to create the vertical axis Darius wind turbine, Lee et al. (2013) created a numerical simulation to analyze the impact of the angle of attack on a NACA 0015 airfoil. The ideal near-wall y^+ value for near-wall modeling is believed to be less than 1. When the velocities and the length of the chord were 43.8 m/s and 0.12 m, respectively, and the Reynolds number was 3.6×10^5, they looked at the best value of y^+ at that Reynolds number. They concluded that using a y^+ value near 1 is appropriate. The coefficient of lift and coefficient of drag result of the numerical analysis of NACA 0012 airfoil with rectangular BCP of width 0.032c at 0.045c for angles of attack ranging from 0° to 16° have been compared and analyzed with the experimental work carried out by Nakamura et al., 2012 for the validity of the study. After validation, the specified objectives are confirmed by simulating and studying the airfoils with BCPs of rectangular cross-section at different locations and of different sizes, and comparing their aerodynamic properties to those of clean airfoils.

3.1 Physical Model

In the current investigation, a symmetrical NACA 0012 airfoil with a 200 mm chord length (c) and a 12 percent thickness was used to evaluate various configurations with burst control plates that had a rectangular cross-section attached to its upper surface. Despite the three-dimensional nature of an aircraft wing, the burst control plate's rectangular cross-section profile is nearly identical in the spanwise direction. In order to keep things simple, the plate may be thought of as being modeled in two dimensions. In the current work, a 2D airfoil geometry with a rectangular BCP has been used. This geometry is set up as a bump and was first proposed by Rinoie et al., 2009.

A schematic 2D representation of the airfoil model with the rectangular burst control plate attached is shown in figure 3.2. The plate is a rectangular bulge on the surface of the airfoil that is quantifiably described by the plate height (h) and width (w). The chord wise distance (shown as X_P) between the front end of the plate and the leading edge of the airfoil determined where the plate should be placed. Note that the distance along the X_C chord line of the airfoil was used to define X_P. In steady state mode, positions 0.045c, 0.05c, 0.07c, and 0.1c from the airfoil leading edge have been studied for

rectangular cross-section BCPs of five sizes: widths of 0.008c, 0.016c, 0.024c, 0.032c, and 0.040c, and a constant height of 0.005c as shown in table 3.1. The study's ultimate goal is to advance knowledge of the aerodynamic properties of airfoils with rectangular burst control plates mounted in a variety of places and sizes.

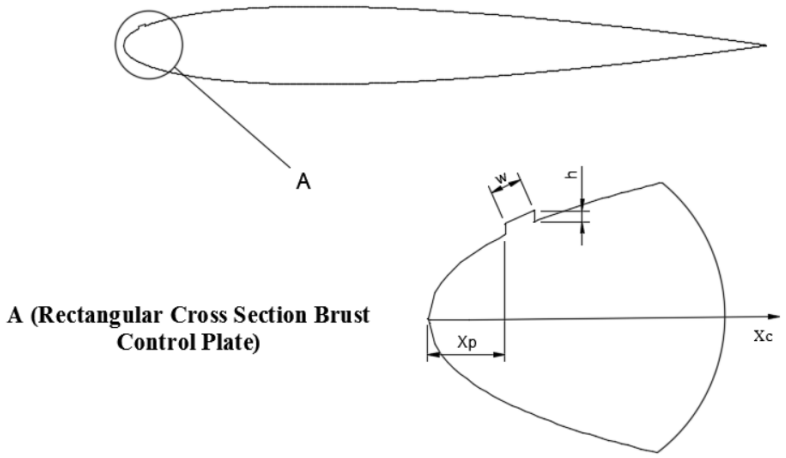

Figure 3.2: Geometric parameters for BCP with rectangular cross-section

Table 3.1: BCPs geometric parameters

Height (H)	Width (W)	Chord wise leading edge plate distance (X_P)
0.005c	0.008c 0.016c 0.024c 0.032c 0.040c	0.045c 0.05c 0.07c 0.1c

3.2 Computational Mesh

The domain has been used is C-type in this research as it is simple and convenient to create block topology, and it is perfect for 2D airfoils with a blunt or sharp trailing edge. The airfoil employed in this study has a chord length (c) of 200 mm and a thickness (t) of 30 mm. The boundaries must be far enough away from the areas of interest in order to prevent interference because the mesh is meant to be used to compute the fluid flow's attributes. The outer boundary is positioned distant from the airfoil to reduce influence of far-field boundary or to enhance the numerical simulations stability. As a result, the current computational domain is of the C-type, with downstream length L = 30c and radius R = 15c, as illustrated in figure 3.3.

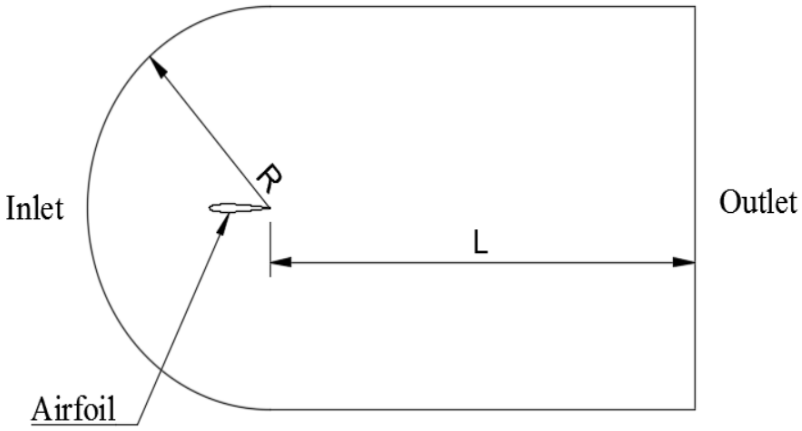

Figure 3.3: The C-type computational domain

The symmetrical shape of NACA 0012 is chosen for the airfoil model in the current investigation to match the wind tunnel measurement data. Here, "00" denotes that there is no camber, and "12" denotes that the chord length to thickness ratio is 12 %. To make it easier to grasp the complicated 3D flow characteristics computationally, the analysis region has been modeled by assuming a 2D shape. The NACA 0012 airfoil was initially designed using the 4-digit series of NACA airfoils from the NACA airfoil database (see Appendix A). An airfoil surface was created in ANSYS FLUENT after the 2D airfoil points were uploaded. FLUENT 2020 R2 has built the structural quadratic C-type mesh displayed in figures 3.4, 3.5 and 3.6. A denser mesh has been adopted nearer to the airfoil surface and around burst control plate where wake are produced. As the mesh density moves away from the airfoil surface, it gradually becomes coarser. The location of the first node in the inflation mesh nearer to the wall is crucial for CFD simulations.

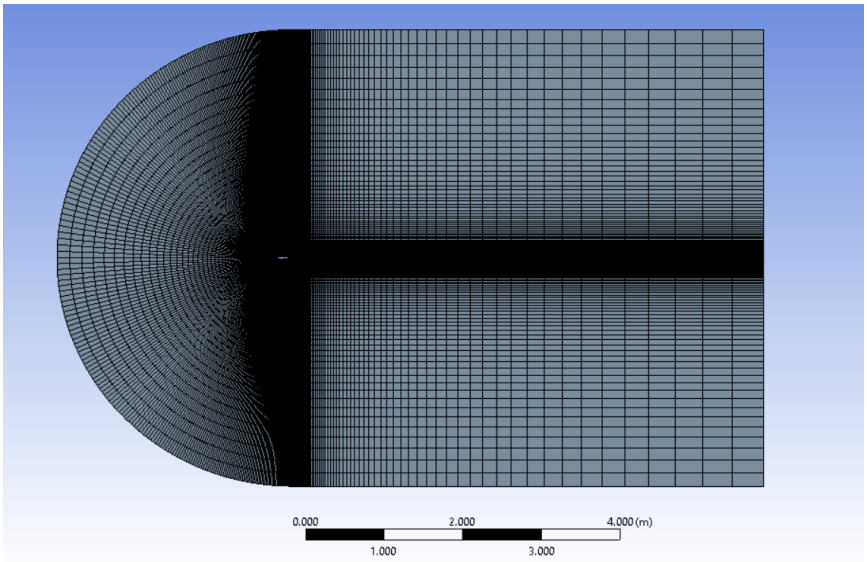

Figure 3.4: Structured mesh of computational domain

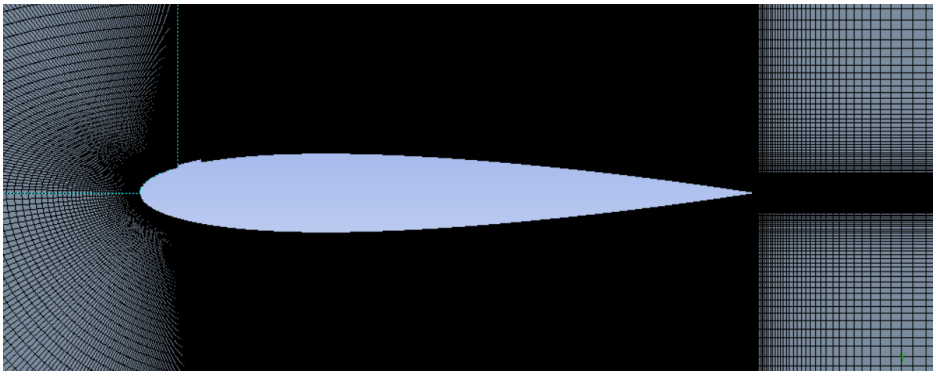

Figure 3.5: Dense mesh near airfoil surface

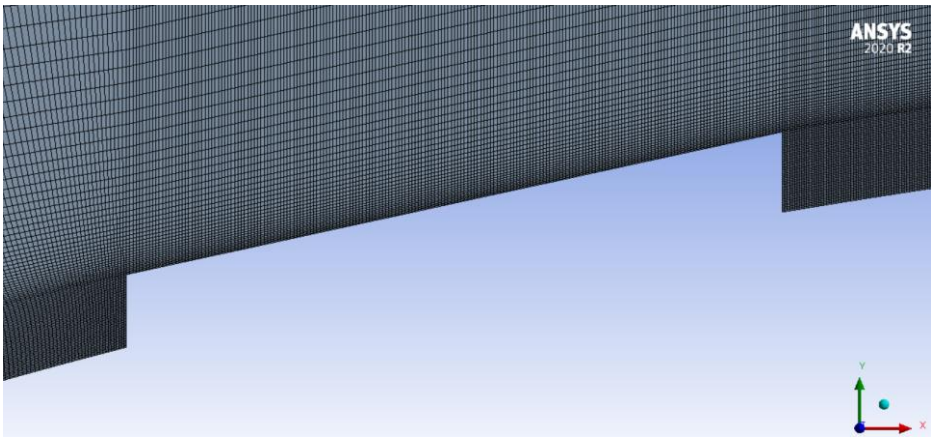

Figure 3.6: Close view of dense mesh near rectangular BCP

The y^+ value represents the dimensionless distance between the mesh's initial node and the wall. y^+ must fall inside a specified range in order to apply a wall function technique properly. The boundary layer region must contain the initial node of the mesh that is perpendicular to the surface. If this doesn't happen, our turbulence model's Wall Functions may use this first calculation point to improperly calculate the flow parameters, which will have an impact on the findings for our velocity and drop in pressure. The y^+ must be specified in order to calculate the wall distance or the distance from the first node to the wall (y). The wall distance (y) is calculated using equation 3.1, equation 3.2, equation 3.3, equation 3.4 and equation 3.5.

$$\text{Wall distance } (y) = \frac{y^+ \mu}{\rho \mu^+} \tag{3.1}$$

$$\text{Friction velocity } (\mu^+) = \sqrt{\frac{\tau_w}{\rho}} \tag{3.2}$$

$$\text{Wall shear stress } (\tau_w) = C_f \frac{1}{2} \rho U_\infty^2 \tag{3.3}$$

$$\text{Reynolds number } (Re_x) = \frac{\rho U_\infty x}{\mu} \tag{3.4}$$

Using Schlichting skin-friction correlation for $Re_x < 10^9$,

$$\text{Skin friction } (C_f) = [2\ log\ Re_x - 0.65]^{-2.3} \quad 3.5$$

Around the airfoil, the mesh is finer to guarantee that y^+ is equal to or less than one for accurate boundary layer flow simulation. Here, Re_x = 1.3×10^5, freestream velocity (U_∞) = 9.45 m/s, density (ρ) = 1.225 kg/m³, dynamic viscosity (μ) = 1.7894×10^{-5} kg/m s and y^+ = 1. Hence, the wall distance has been calculated to be 3.1×10^{-5}m. The wall distance can also be calculated from CFD online website that has y^+ wall distance estimation tool (see Appendix B).

3.3 Boundary Conditions and Solver Setup

The computational domain's front, upper, and bottom boundaries were set as velocity inlets, the back boundary as a pressure outlet, and the airfoil boundary as a no-slip wall. The Transition SST turbulence model was selected.

After the meshes are finished, the simulation setup can begin. Meshes are used by FLUENT to model the fluid space. The computation was done using the commercial program ANSYS FLUENT 2020 R2, which uses the finite volume approach. At each node of the mesh, ANSYS FLUENT numerically solves the Navier-Stokes equations. FLUENT employs an iterative approach to converge case solution.

The solver has a steady state setting. The solver adopted is pressure based as incompressible flow is assumed. Pressure, viscosity, and density are considered as they would be at sea level. At 1%, the turbulence intensity is set. To obtain the appropriate Reynolds number (R_e) and value of y^+ less than 1, the input freestream velocity was predetermined and set to 9.45 m/s. Pressure-velocity coupling algorithm SIMPLE (semi-implicit method for pressure-linked equations) and finite volume approach for discretizing RANS equations were used. Calculation uses second-order upwind spatial discretization. Cell-based least squares are used to choose the spatial gradient. Target values for residual convergence criterion were set at 10^{-7}.To find drag coefficient at different angle of attacks, the x component force vector is put in the form cosα and y component force vector is put in the form sinα and for lift coefficient at different angle of attacks, the x component force vector is put in the form -sinα and y component force vector is put in the form cosα.

3.4 Mesh Independence Study

The process of generating mesh is one of the crucial process in numerical analysis for CFD. The mesh's design and the number of cells have a general impact on the simulation's conclusions. If there are more cells, the solutions will be more accurate, but this could take longer and have an influence on memory limitations. To do simulations, a coarse mesh should be created first. Then the mesh are made finer for more precise solution. If mesh independence is attained then the mesh is used for further simulation if it produces a solution that is similar with the finer meshes.

In order to test mesh independence, six different meshes with increasing number of elements were utilized: 163,600 cells, 284,000 cells, 408,400 cells, 566,400 cells, 683,000 cells and 1,022,393 cells for the airfoil with BCP of width 0.040c at position 0.1c with an angle of attack (α) = 8°. Figure 3.7 shows the lift coefficients (C_L) of an airfoil with a burst control plate at Reynolds number 1.3×10^5 for different number of mesh elements. Table 3.2 shows the error percent of 0.136% in lift coefficient when the element number is increased from 284,000 to 408,400, which is less than 1% and fall in the acceptable range. So, 408,400 mesh was used for computation in this paper.

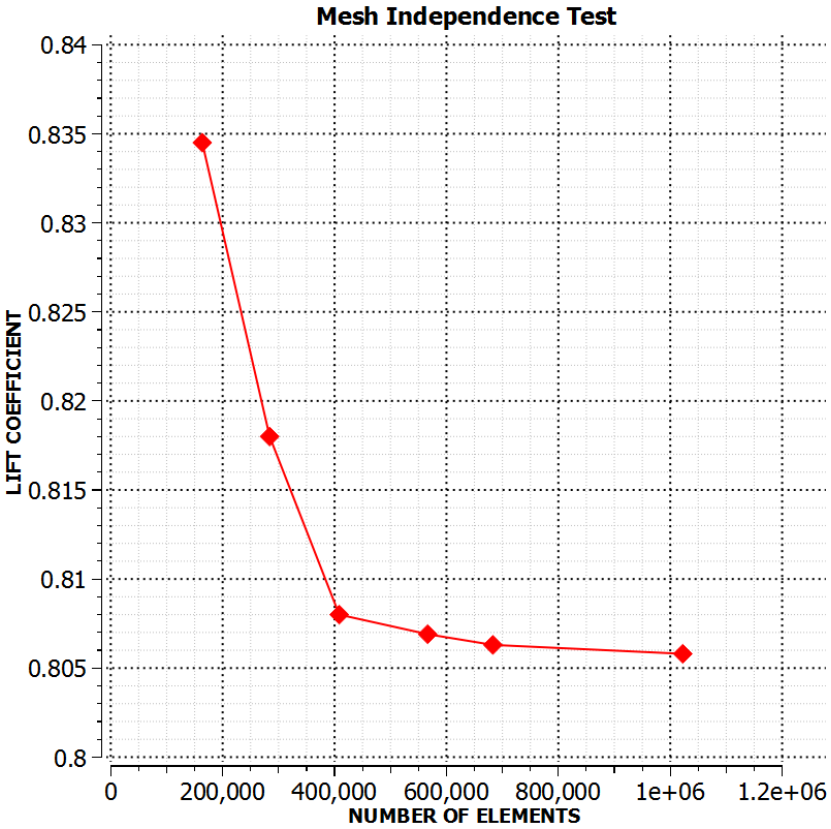

Figure 3.7: Lift coefficient versus number of elements at α = 8^0

Table 3.2: Error percent in lift coefficient for angle of attack 8°

Number of Element	Coefficient of Lift	Error Percent (fine element C_L - coarse element C_L) / fine element C_L×100%
163600	0.8345	2.017114914
284000	0.818	1.237623762
408400	**0.808**	**0.136324204**
566400	0.8069	0.07441399
683000	0.8063	0.062050137
1022393	0.8058	

3.5 Mesh Quality

Figure 3.8 shows the number of elements for the setup which is 408400. The quality of finalized mesh is checked through mesh metrics after mesh independence test. Three mesh metrics are taken for determining the mesh health, which are: Skewness, Jacobian ratio and Orthogonal quality.

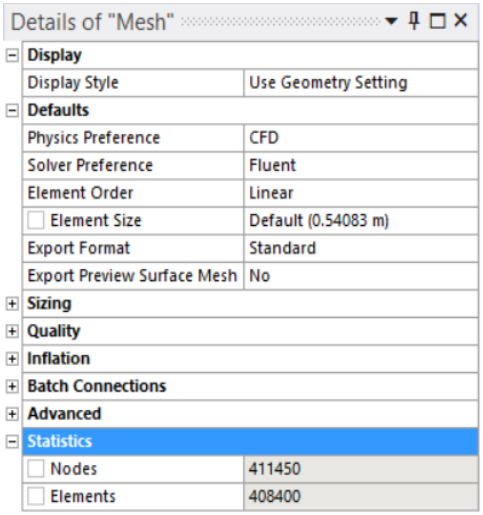

Figure 3.8: Number of nodes and elements

3.5.1 Skewness

The difference between the shape of the cell and the shape of an equilateral cell with an equivalent volume is defined as skewness. Highly skewed cells might make the solution unstable and reduce accuracy. It is an index of how close the value is to the ideal shape. It is a scale between 0 to 1. The average skewness 0 means best and 1 means worst. A maximum skewness of less than 0.5 and an average of 0.1 are desirable

for 2D. The obtained average skewness of finalized mesh is 0.088316 with maximum skewness of 0.46 as shown in figure 3.9. Figure 3.10 illustrates the number of elements of the corresponding skewness quality. It shows major number of elements have low skewness between 0 and 0.1.

Mesh Metric	Skewness
Min	1.3057e-010
Max	0.46683
Average	8.8316e-002
Standard Deviation	0.10155

Figure 3.9: Skewness quality

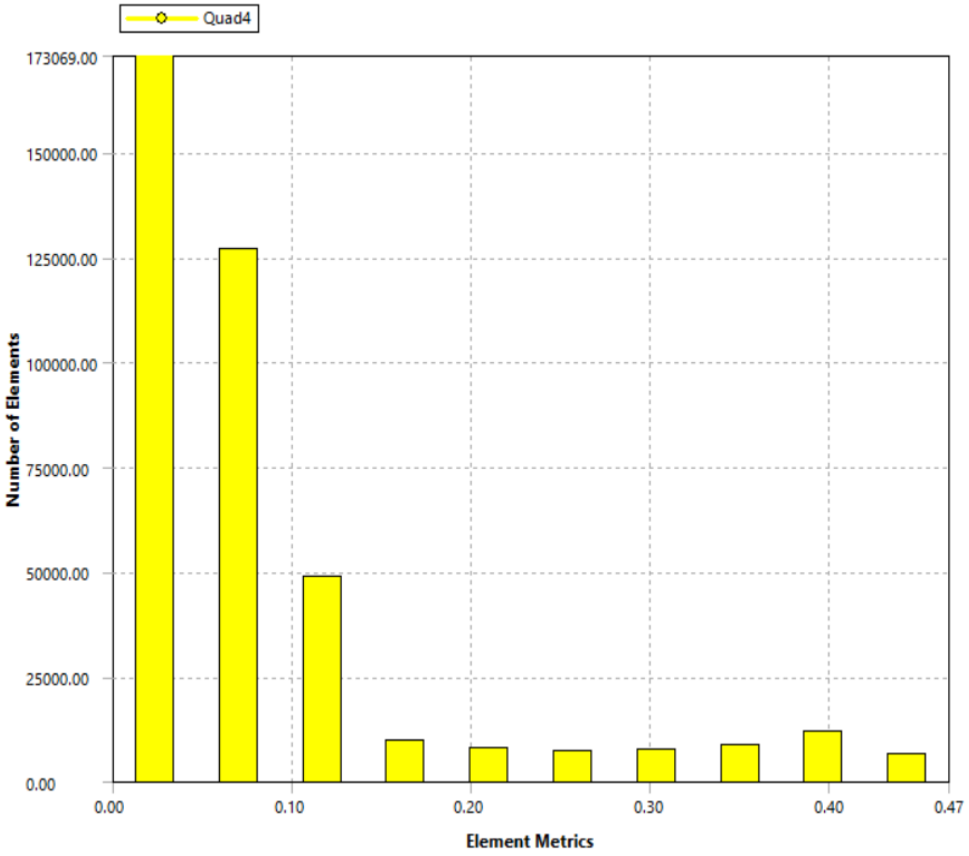

Figure 3.10: Elements number versus skewness quality

3.5.2 Jacobian ratio

The Jacobian ratio calculates how far an element deviates from being perfectly formed (one that has straight edges with equal lengths). It is a scale between 1 to 10. The average Jacobian ratio 1 means best and 10 means worst. A perfect second order tetrahedral element with linear edges has a Jacobian ratio of one. The obtained average Jacobian ratio of finalized mesh is 1.0032 with maximum Jacobian ratio of 1.0961 as shown in figure 3.11. Figure 3.12 illustrates the number of elements of the

corresponding Jacobian ratio. It shows major number of elements have low Jacobian ratio between 1 and 1.01.

Mesh Metric	Jacobian Ratio (MAPDL)
Min	1.
Max	1.0961
Average	1.0032
Standard Deviation	1.3795e-002

Figure 3.11: Jacobian ratio quality

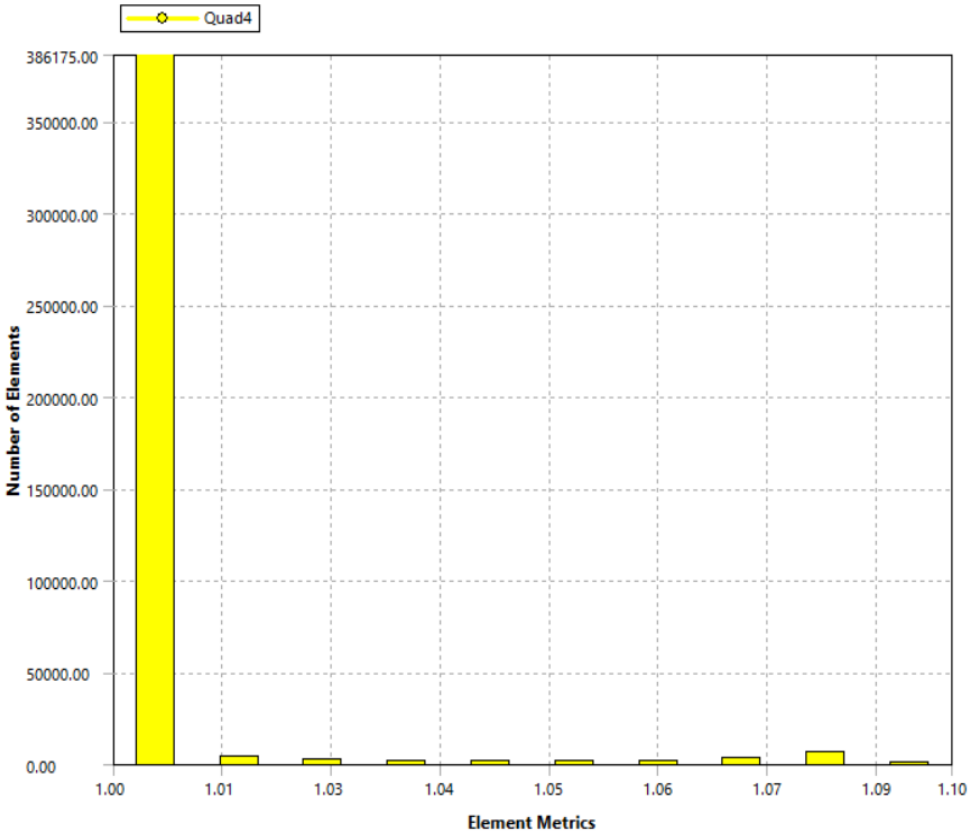

Figure 3.12: Elements number versus jacobian ratio

3.5.3 Orthogonal quality

The degree to which the angles between consecutive element faces (or adjacent element edges) are close to an ideal angle is referred to as mesh orthogonality (depending on the relevant topology). It is a scale between 0 to 1. The average Orthogonal quality 0 means worst and 1 means best. An average orthogonal quality of 0.5 is considered to be acceptable. The obtained average Orthogonal quality of finalized mesh is 0.97682 with maximum Orthogonal quality of 1 as shown in figure 3.13. Figure 3.14 illustrates the number of elements of the corresponding Orthogonal quality. It shows major number of elements have high Orthogonal quality between 0.95 and 1.

Mesh Metric	Orthogonal Quality
Min	0.60599
Max	1.
Average	0.97682
Standard Deviation	5.0584e-002

Figure 3.13: Orthogonal quality

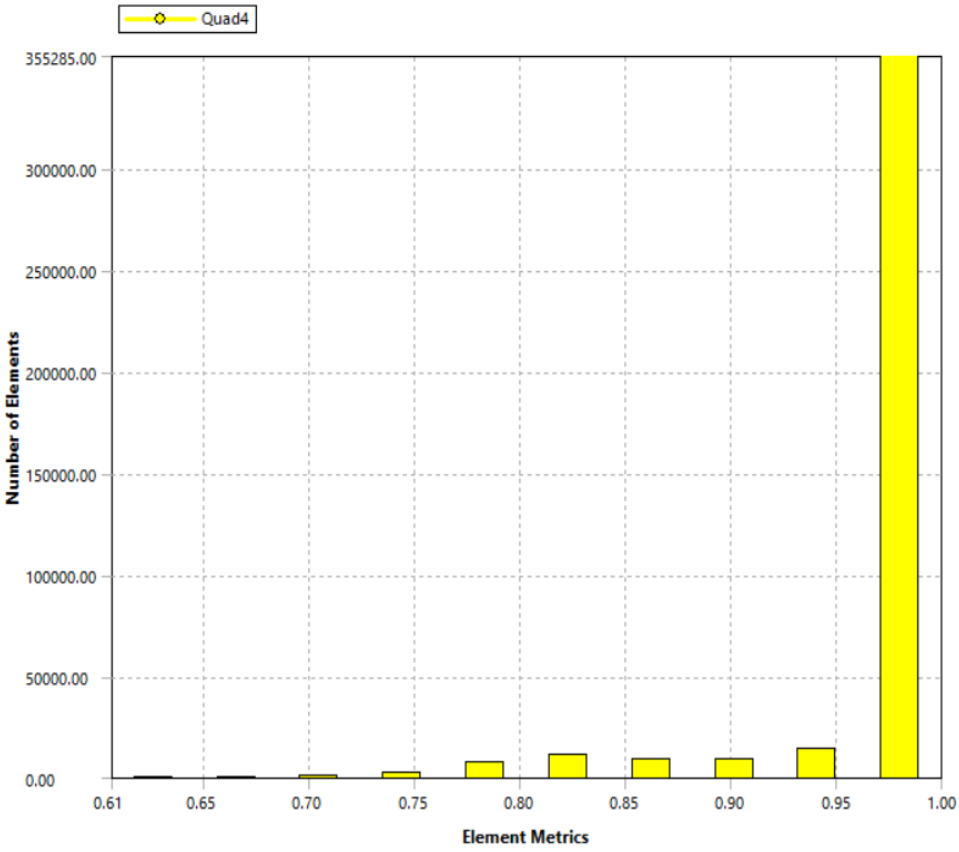

Figure 3.14: Elements number versus orthogonal quality

CHAPTER FOUR: RESULTS AND DISCUSSION

4.1 Model Validation

Burst control plates of five different widths were numerically analyzed at four different locations on NACA 0012 airfoil at Reynolds number 1.3×10^5 for the current study. Out of 20 different configurations which were numerically analyzed, one configuration matches the experimental analysis carried out by Nakamura et al., 2012. Nakamura et al., 2012, tested NACA 0012 airfoil of 200 mm chord length(c) with plate configuration of height(h/c) 0.005, width(w/c) 0.032c, and leading-edge position(X_P/c) 0.045c, in a low-speed suction type wind tunnel of height 600mm, width 200mm and length 1000mm. And measurements were taken at a free stream velocity of 10m/s with turbulence intensity less than 0.16% at the Reynolds number of 1.3×10^5. Flow visualization pictures were obtained by the Particle Image Velocimetry (PIV) system to understand the flow pattern around the plate. The experimental data, used here for comparison, are the measured lift coefficients for validation of the model.

Validation is carried out to make sure that the numerical approach and solution methods chosen for the current problem accurately forecast the physics. Shrestha et al., 2019, have concluded the Transition SST model to be the best turbulence model in ANSYS FLUENT for numerical analysis of flow separation on a clean airfoil. So, Transition SST turbulence models are used for the numerical analysis on NACA 0012 airfoil of 200 mm chord length with burst control plate of width 0.032c at leading edge position of 0.045c.

In figure 4.1, the computed lift coefficients (C_L) of flow past an airfoil with a burst control plate at various angles of attack ranging from 0° to 16° with 2° interval have been compared with clean airfoil at the Reynolds number of 1.3×10^5 and the experimental data of Nakamura et al., 2012. Large gap can be seen between experimental data and numerically analyzed data for angle of attack greater than 6°. While both experimental data and numerical analyzed data follow same pattern for lift coefficient. However, these pattern are different from lift coefficient pattern of clean airfoil. The graph also shows that numerically analyzed data are greater than experimentally obtained data for lift coefficient of airfoil with BCP at all angle of attack.

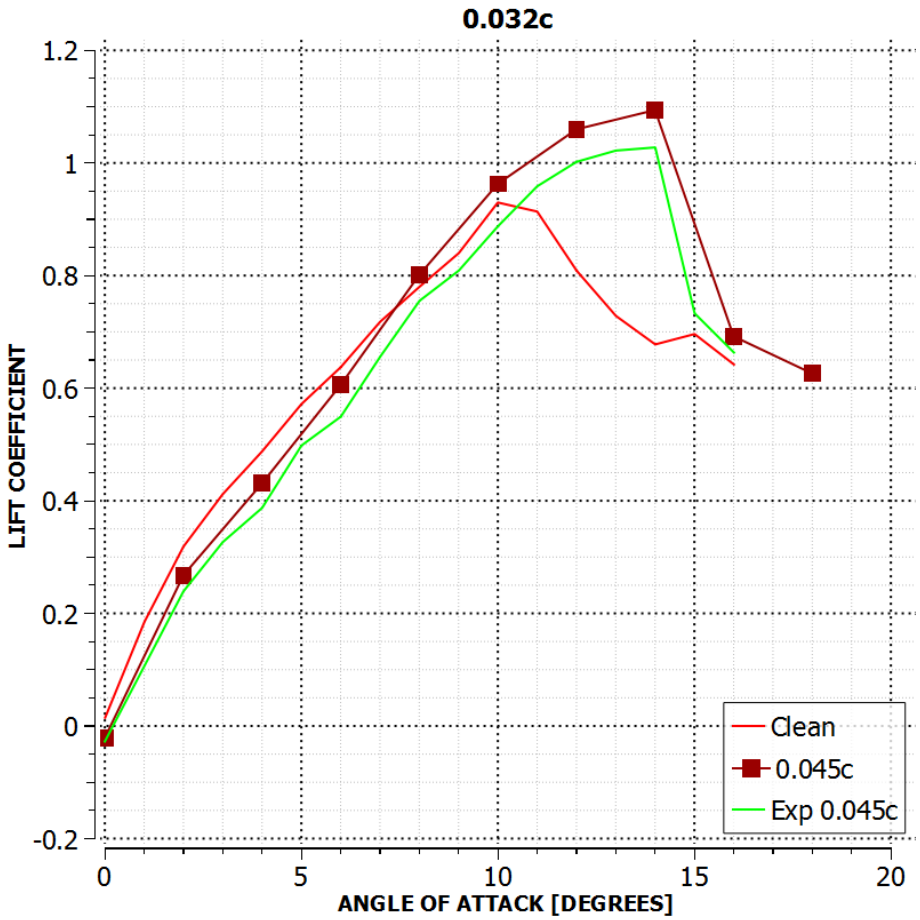

Figure 4.1: Lift coefficient versus angle of attack

Particularly in the pre-stall zone, the simulation findings of Transition SST turbulence models used for numerical analysis are close to the experimental result, which is further supported by Table 4.1. For unstable flow RANS modelling's have limitations at stalled situations due to which numerical findings in the stall zone do not always show totally satisfactory results. The simulation that was done on ANSYS FLUENT is a 2D setup, although a wind tunnel is also a 3D setup. As a result, the wind tunnel detects 3D impacts that ANSYS FLUENT does not take into consideration in the current work. These factors could result in greater lift and greater drag than typical.

It is clear that the Transition SST model used for numerical analysis produced the least amount of divergence. As an illustration, it was capable to record the maximum lift of 1.094 at angle of attack (α) = 10°. Up to this point, the lift coefficient curve had a linear trend. Up to this maximum value, it shows that the flow is still attached, and the subsequent decrease in value denotes detached flow or stall. Table 4.1 shows the average deviations of 9.847% in lift coefficient for the angles between 0° and 16°, between experimental results and results of numerical analysis using Transition SST

model, which is less than 10% and fall in the acceptable range. Similarly, the deviation in lift coefficient is 12% for the angles between 0° and 10° while the deviation is 5.528% for the angles between 12° and 16°. The error may have resulted from the interaction of several numerical techniques and mesh density.

Table 4.1: Error percent in lift coefficient for AOA 0°-16°

Angle of Attack	**Experimental value**	**Numerical Analysis value**	**Error percent**
0°	-0.028	-0.021	23.88546575
2°	0.239	0.268	12.02108081
4°	0.387	0.431	11.27375052
6°	0.549	0.606	10.25062337
8°	0.755	0.801	6.088695261
10°	0.887	0.963	8.524161558
12°	1.002	1.060	5.765469062
14°	1.028	1.094	6.487023034
16°	0.663	0.692	4.331895902
		Average Error Percent	
			9.847573918

The results thus demonstrate that the Transition SST turbulence model cannot represent the flow as effectively as expected due to the substantial adverse pressure gradient, which has a considerable impact on the flow property leading to separation of flow. It is advised to use more efficient alternative numerical analysis model, like DNS, DES, and LES for the flow simulation to get more accurate results, however, these are time consuming and require huge memory.

4.2 Investigation of coefficient of pressure plots

Various sizes rectangular cross-section BCPs at different positions were used in the computations to examine the effect on flow around NACA 0012 airfoil. At 0.045c, 0.05c, 0.07c, 0.1c from the leading edge of NACA 0012 airfoil, five BCPs with widths of 0.008c, 0.016c, 0.024c, 0.032c and 0.040c were examined.

Figures 4.2 and 4.3 illustrate distribution of pressure along the surface of clean airfoil and an airfoil with BCP positioned at 0.045c and of width 0.032c respectively. With the clean airfoil for $\alpha = 10°$, the figure shows that a short bubble was created (note toward the leading edge of airfoil the strong suction pressure, succeed by a flat area and a sharp recovery of pressure, which denotes reattachment of flow). With the clean

airfoil, when α was raised from 10° to 12°, there is a loss of negative coefficient of pressure, indicating that the airfoil has stalled. When α was raised to 14° for this airfoil, both the strong suction pressure toward the leading edge of airfoil and sharp recovery of pressure were completely removed. At α = 14°, a high suction pressure peak was seen for the airfoil with BCP, indicating stall suppression. As angle of attack is increased to 16° the peak of negative suction pressure falls. Figures also indicate that for same angle of attack, an airfoil with BCP has reduced coefficients of pressure (C_P) when compared to a clean airfoil. So, the area inside curve is increased for airfoil with burst control plate compared to clean airfoil at same angle of attack. A sharp rise in coefficients of pressure (C_P) at chord position 0.045c indicates a sudden decrease in pressure due to the presence of BCP.

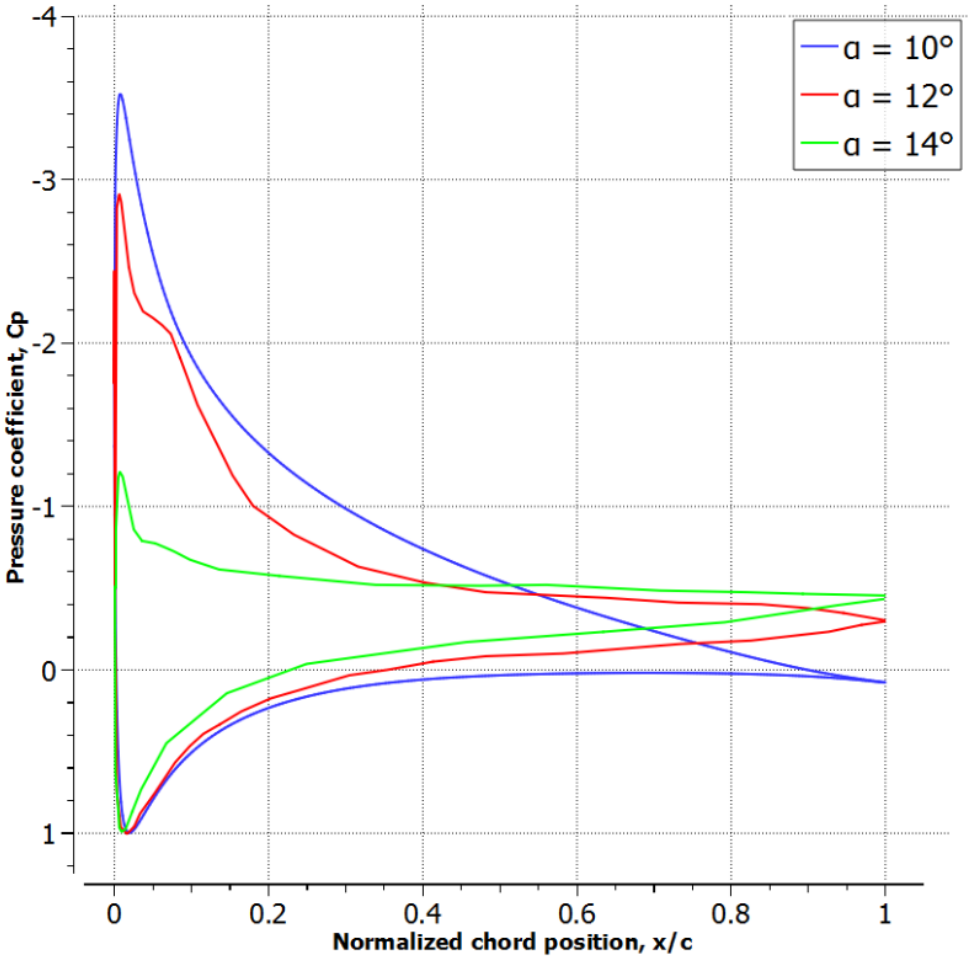

Figure 4.2: Pressure coefficient distributions with variations of α for clean airfoil

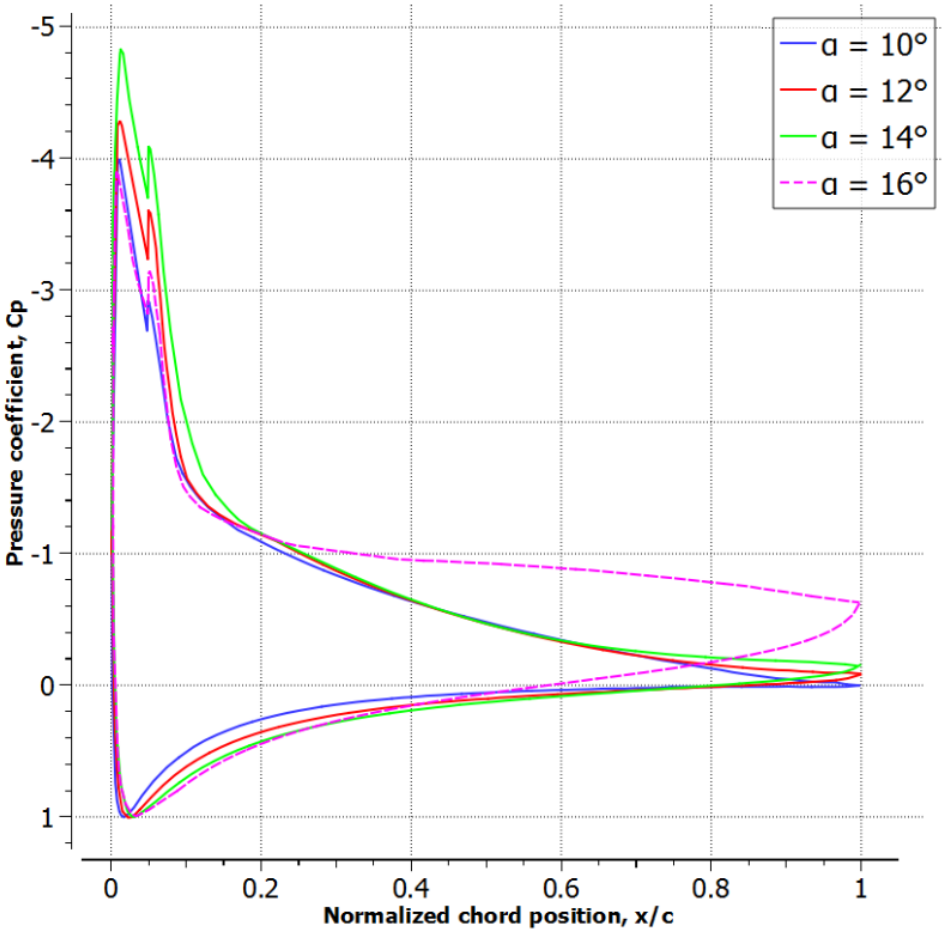

Figure 4.3: Pressure coefficient distributions with variations of α for 0.032c width BCP at 0.045c location

As a result, it is clear that the stall angle has been suppressed or delayed from 10° to 14°, which supports the burst control plate's effectiveness in reducing stall.

4.3 Effects of plate size located at various positions on the aerodynamics of airfoil

The lift coefficients (C_L) and drag coefficient (C_D) curves of clean NACA 0012 airfoil (baseline study-Transition SST model) and same airfoil with rectangular cross-section BCPs of widths 0.008c, 0.016c, 0.024c, 0.032c and 0.040c positioned with respect to the leading edge at 0.045c, 0.05c, 0.07c and 0.1c of the airfoil are shown in figures 4.4-4.13.

First, a plate of constant width 0.008c has been simulated at different positions of 0.045c, 0.05c, 0.07c, and 0.1c from the airfoil leading edge, in order to investigate the effects of BCPs with rectangular cross-section at different positions of airfoil for different sizes. The lift coefficient (C_L) vs. angle of attack (α) graph shows that when the angles of attack is less than 6°, airfoil with BCPs shows lower C_L than clean airfoil

for all positions. Between 6° and 18° airfoil with BCPs shows a greater value of C_L. At maximum stall angle α = 12° for an airfoil with BCP of width 0.008c placed at 0.05c position, the maximum lift coefficient is 1.04734, which is over 12.64% greater than the maximum lift coefficient of the clean airfoil (0.92978) at α = 10° for $R_e = 1.3\times10^5$. The Stall angle is suppressed to 12° for an airfoil with BCP at all positions.

In addition, if we look at the graph of the drag coefficient (C_D) versus angle of attack (α), for angle of attack less than 8°, C_D is more for an airfoil with BCP at all positions when compared to the airfoil with no BCPs. This increase in drag is due to skin friction. Drag is effectively reduced when the angles of attack are between 8° and 18° for an airfoil with BCP at all positions. At stall angle (α) = 12°, the minimum coefficient of drag is 0.046 for BCP width 0.008c at position 0.1c, which compared to clean airfoil is 44.44% reduction in drag.

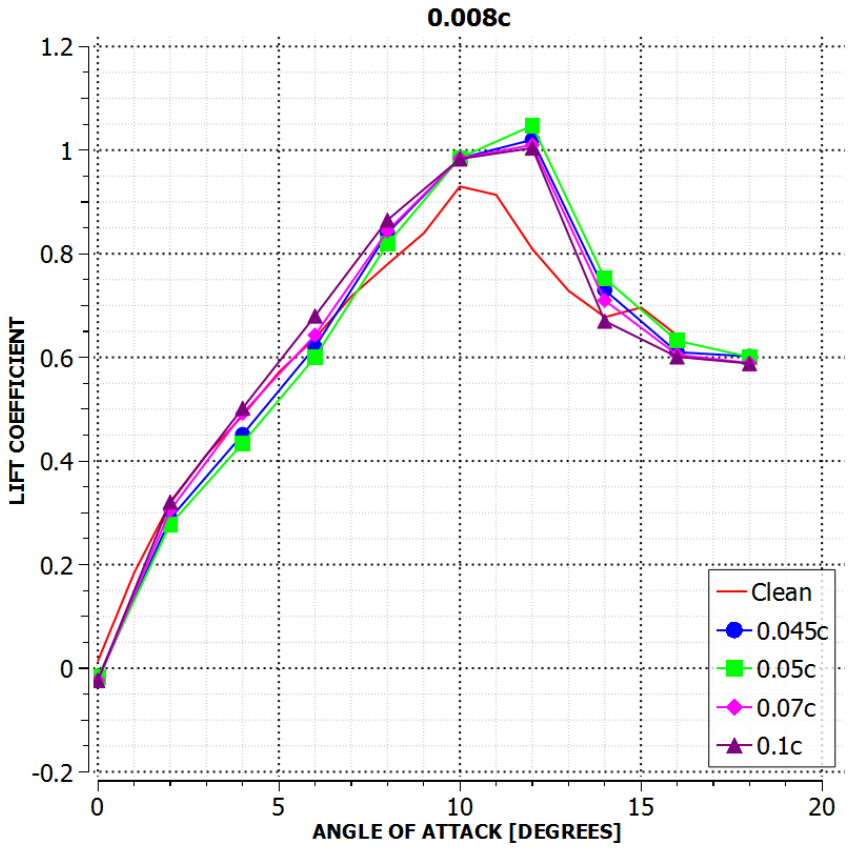

Figure 4.4: Lift coefficient versus angle of attack for 0.008c width

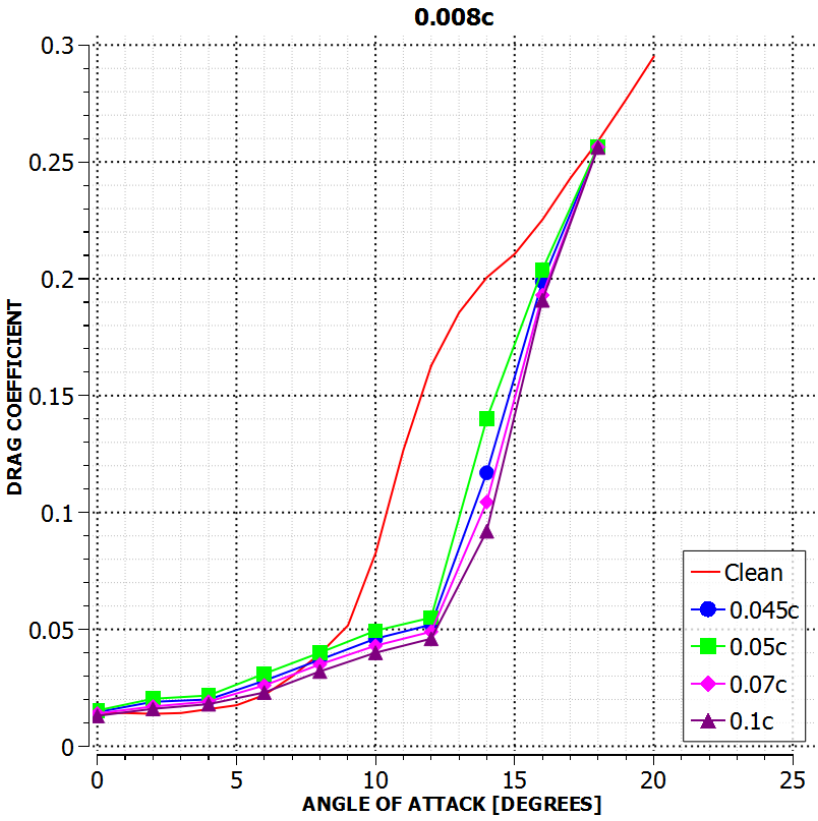

Figure 4.5: Drag coefficient versus angle of attack for 0.008c width

The 0.016c width BCP depicts pattern for C_L and C_D curves similar to the 0.008c width BCP. For the BCP width 0.016c, the coefficient of lift versus angle of attack curve shows that the value of C_L for airfoil with burst control plate are less than airfoil without BCP for angle of attack less than 6° at all positions. Above 6° angle of attack, the computed C_L values are higher for airfoil with BCP than clean airfoil. Also, we can observe that the stall angle has been delayed from 10° to 12° for all positions. In addition, at stall angle α = 12°, the maximum C_L value of 1.06 is computed for the airfoil with BCP plate placed at 0.05c position, which is 14% greater than the maximum C_L value of 0.92978 at α = 10° for clean airfoil.

The coefficient of drag (C_D) versus angle of attack (α) graph indicates the higher value of C_D at α < 8°, for all positions of airfoil with BCP while beyond this angle of attack, the C_D values are less when compared to clean airfoil. The C_D values computed for 0.1c position are less than for other positions at every angles of attack. In particular, the maximum reduction in C_D value is 38.40% at α = 12° for the 0.016c width plate placed at 0.1c position in comparison to C_D of clean airfoil.

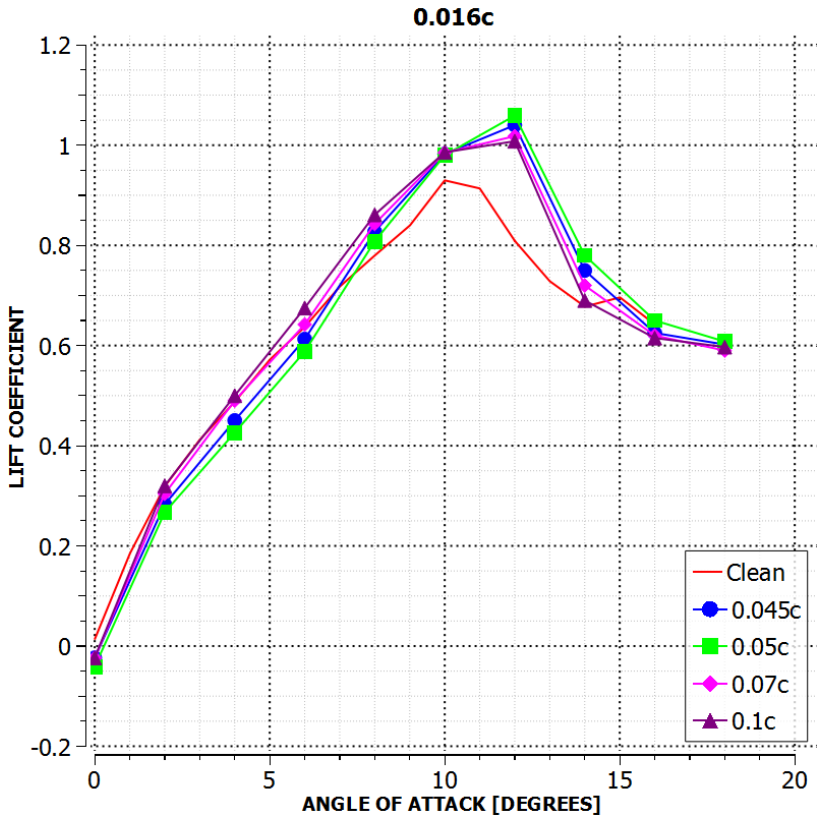

Figure 4.6: Lift coefficient versus angle of attack for 0.016c width

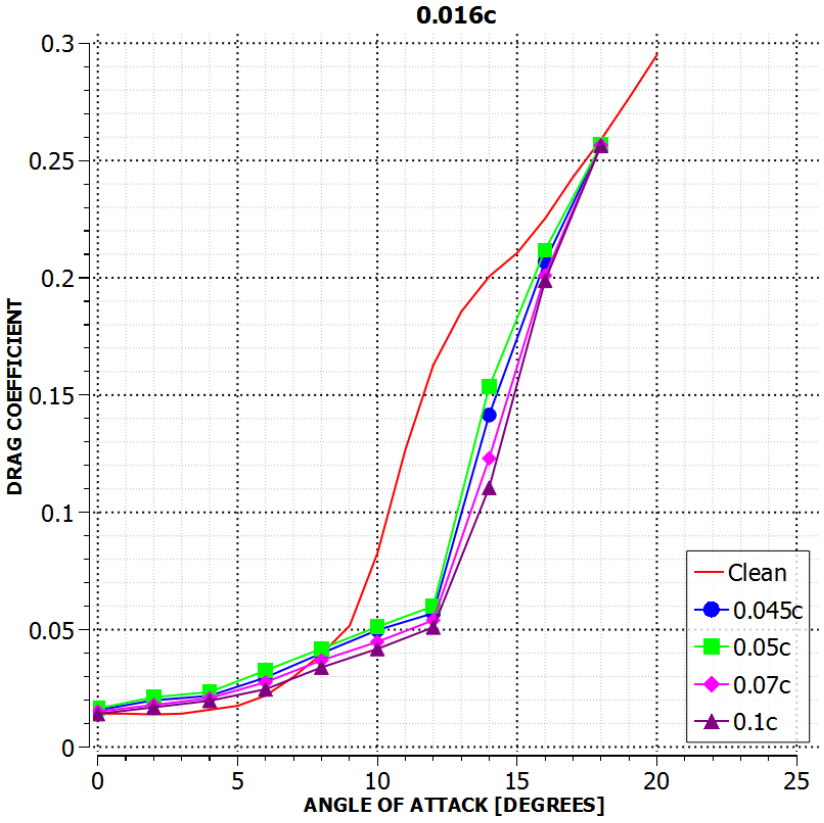

Figure 4.7: Drag coefficient versus angle of attack for 0.016c width

The 0.024c width BCP shows similar trends as 0.008c and 0.016c width BCP for C_L and C_D curves. When α < 6°, the C_L values are computed less than for clean airfoil for all positions. Beyond α = 6°, the C_L values are greater than for clean airfoil for all positions. In the case of the 0.024c width BCP too, the stall angle has been postponed from 10° to 12° for all positions. In particular, the maximum C_L value of 1.062 is computed at α = 12° is computed for the plate placed at 0.05c position, which is 14.22% greater than the maximum C_L value of 0.92978 at α = 10° for clean airfoil.

For 0.024c width BCP, the C_D values are computed higher by a small margin for all positions for α < 8° when compared to clean airfoil, and beyond this angle of attack, the values are less. The C_D values computed for 0.1c position are lower than for other positions for almost all angles of attack. In particular, the maximum reduction in C_D value from the corresponding baseline value is 36% at α = 12° for the 0.024c width plate placed at 0.1c position.

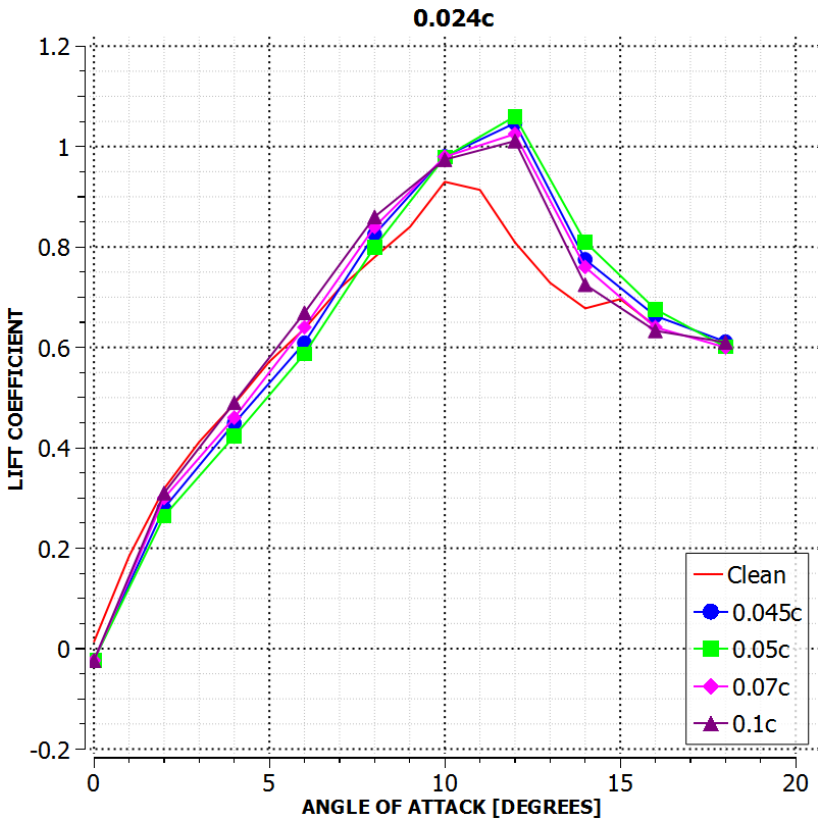

Figure 4.8: Lift coefficient versus angle of attack for 0.024c width

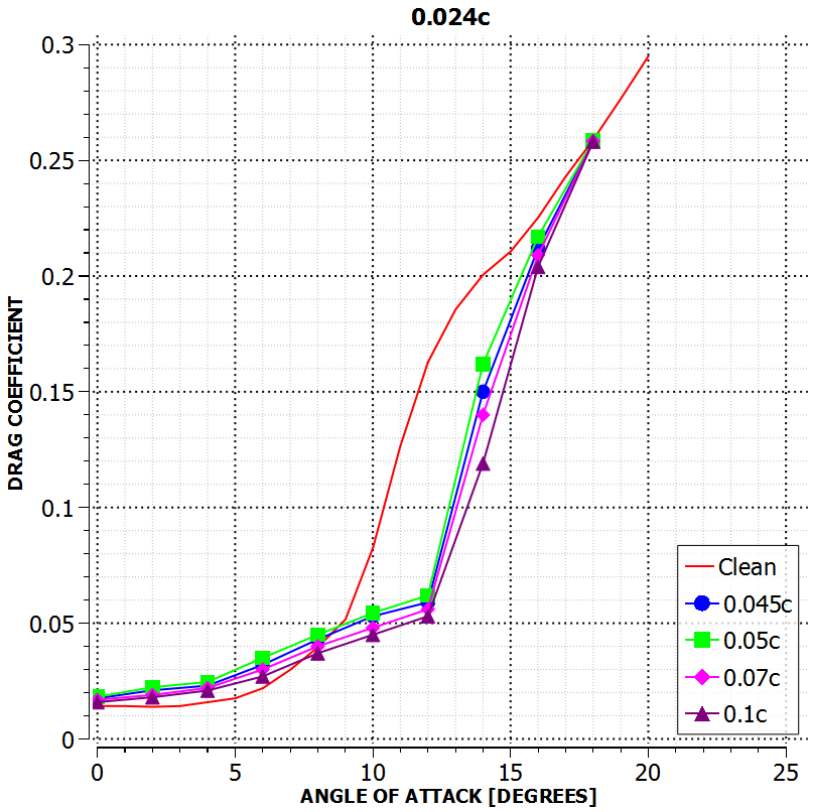

Figure 4.9: Drag coefficient versus angle of attack for 0.024c width

Similarly, the 0.032c width BCP is simulated at the positions 4.5%, 5%, 7%, and 10% of chord(c) from the leading edge of the airfoil. Up to α = 6°, the C_L values are computed less for all positions when compared to clean airfoil. Beyond α = 6°, the computed C_L values are higher than the baseline data. In the case of 0.032c width BCP, the stall angle has been postponed from 10° to 12° for the positions 0.07c and 0.1c. And for positions 0.045c and 0.05c, the stall angle has been suppressed to 14°. In particular, the maximum C_L value is 1.125 at α = 14° computed for 0.05c position, which is 21% more than C_L of clean airfoil at α = 10°.

When we observe the drag coefficient (C_D) versus angle of attack (α) graph, the C_D values are computed higher for all positions up to α = 8°, and beyond this angle of attack the values are computed less when compared to clean airfoil. The C_D values computed for 0.1c position are lower than for other positions for almost all angles of attack. The stall angle for position 0.07c and 0.1c is 12°, and the maximum reduction in C_D value from the corresponding baseline value is 30% at α = 12° for the 0.032c width plate placed at 0.1c position. When BCP position is at 0.045c and 0.05c, the stall angle is 14°. And the minimum C_D value 0.0745 which is 10% smaller than corresponding baseline value is observed at BCP position 0.045c.

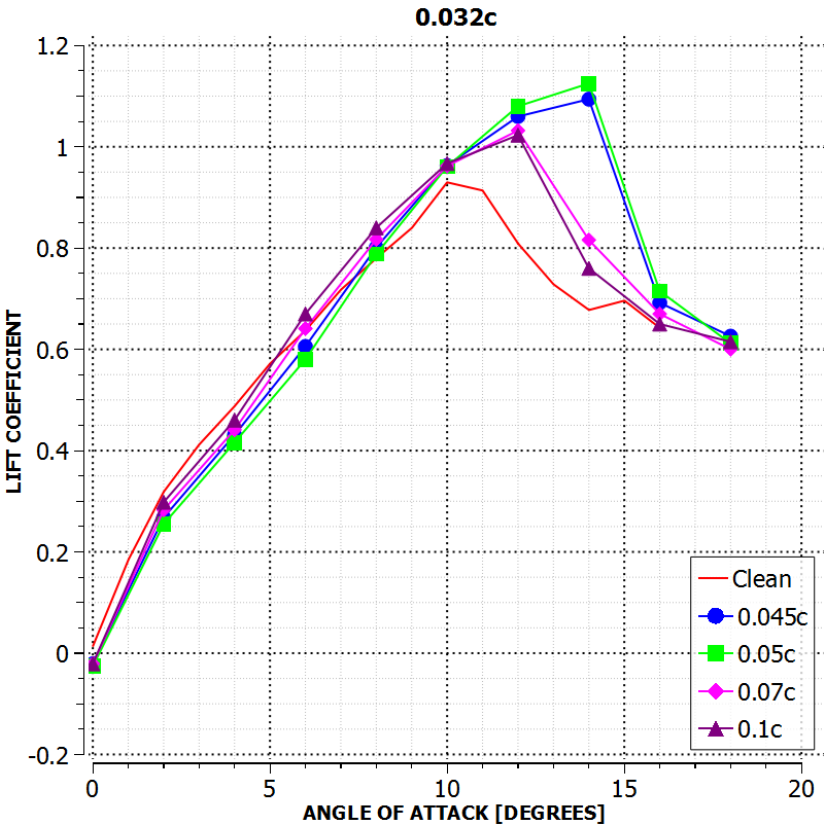

Figure 4.10: Lift coefficient versus angle of attack for 0.032c width

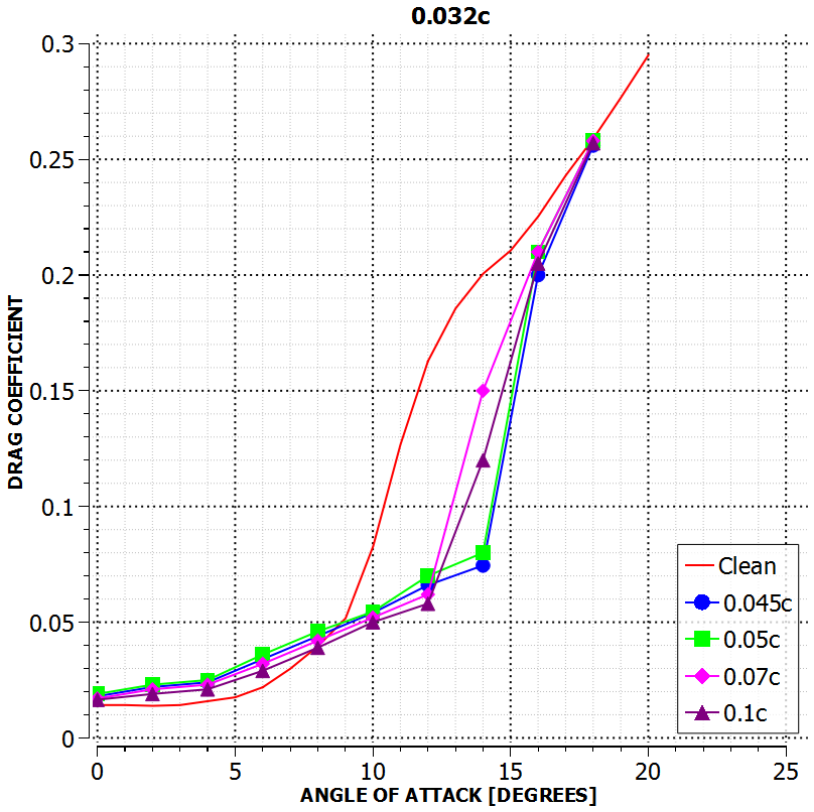

Figure 4.11: Drag coefficient versus angle of attack for 0.032c width

Finally, the 0.04c width BCP is simulated at the positions 4.5%, 5%, 7%, and 10% of chord (c) from the leading edge of the airfoil. The 0.04c width BCP shows similar trends as 0.032c width BCP for C_L and C_D curves. Up to α = 6°, the C_L values are computed less for all positions when compared to clean airfoil. Beyond α = 6°, the computed C_L values are higher than the baseline data. Also, in the case of 0.04c width BCP, the stall angle has been postponed from 10° to 12° for the positions 0.07c and 0.1c. And for positions 0.045c and 0.05c, the stall angle has been suppressed to 14°. In particular, the maximum C_L value is 1.129 at α = 14° computed for 0.05c position, which is 21.426% more than C_L of clean airfoil at α = 10°.

When we observe the drag coefficient (C_D) versus angle of attack (α) graph, the C_D values are computed higher for all positions up to α = 8°, and beyond this angle of attack the values are computed less when compared to clean airfoil. The C_D values computed for 0.1c position are lower than for other positions for almost all angles of attack. The stall angle for position 0.07c and 0.1c is 12°, and the maximum reduction in C_D value from the corresponding baseline value is 26.8% at α = 12° for the 0.04c width plate placed at 0.1c position. When BCP position is at 0.045c and 0.05c, the stall angle is 14°. And the minimum C_D value 0.08 which is 3.38% smaller than corresponding baseline value is observed at BCP position 0.045c.

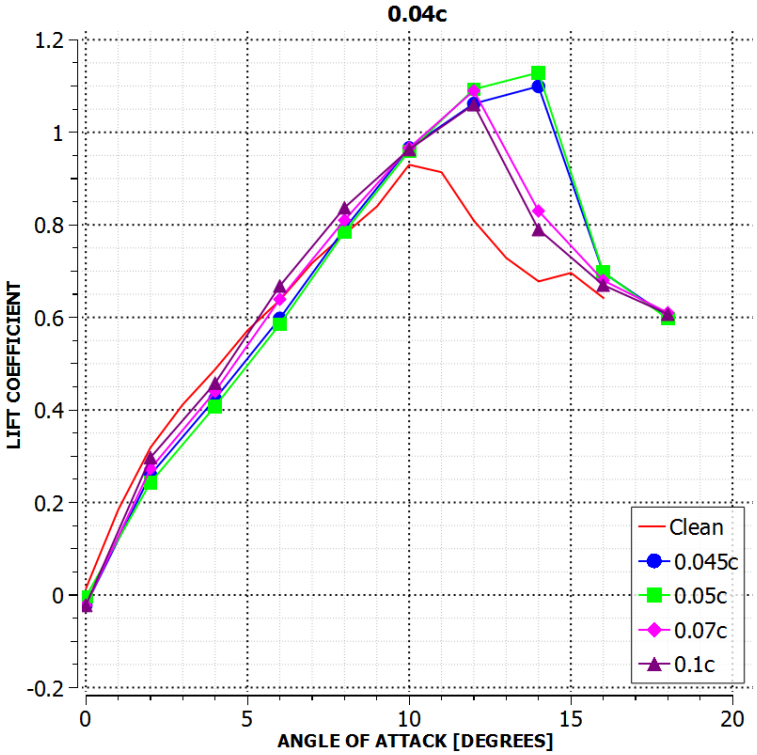

Figure 4.12: Lift coefficient versus angle of attack for 0.040c width

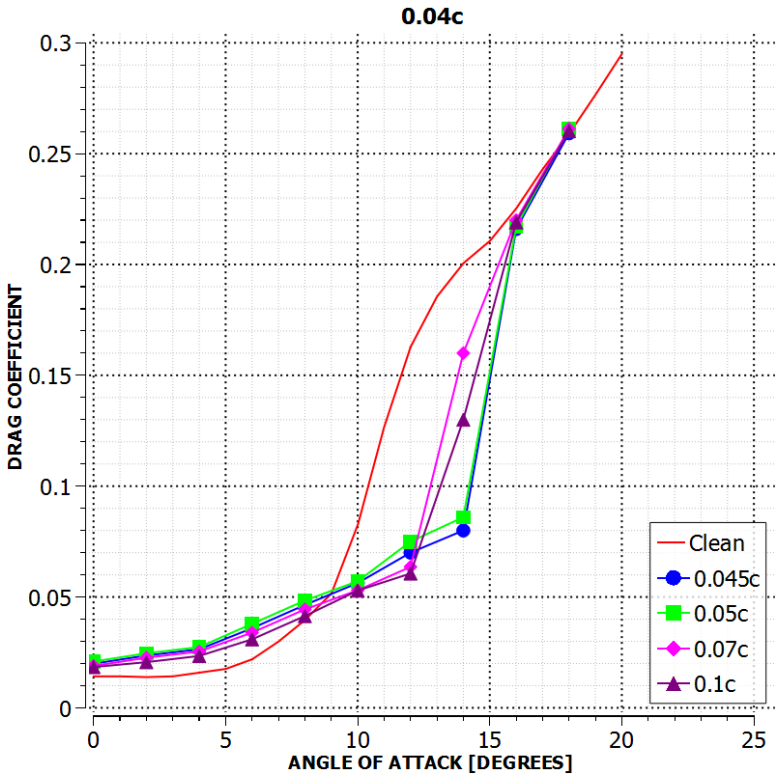

Figure 4.13: Drag coefficient versus angle of attack for 0.040c width

The results, in summary, shows that BCPs of all widths for all positions have given lower coefficient of lift (C_L), when compared to the airfoil without for angles of attack, less than 6°. When the angles of attack are between 6° and 18°, the C_L values for airfoil with BCPs of all widths are greater than the C_L value of the clean airfoil at all locations.

Hence from the study, it can be concluded that for angles of attack greater than 6°, BCPs can improve the characteristics of stall for all configurations because of a smooth reduction in lift coefficient values post-stall angle. Among five widths (0.008c, 0.016c, 0.024c, 0.032c and 0.04c) that are numerically tested in this study, the first three widths 0.008c, 0.016c and 0.024c (where c represents chord length of airfoil used) suppressed stall angle from 10° to 12° at all four positions (0.045c, 0.05c, 0.07c and 0.1c). While rest of the two widths 0.032c and 0.04c suppressed stall angle from 10° to 14° at position 0.04c and 0.05c. And for same widths the stall is suppressed from 10° to 12° at position 0.07c and 0.1c. The maximum value of C_L at a stall angle of 12° for burst control plates (BCPs) of width 0.008c, 0.016c and 0.024c at the location 0.05c are 1.04734, 1.06 and 1.062, which are over 12.64%, 14% and 14.22% higher than the maximum lift value of 0.92978 (at $\alpha = 10°$) of clean airfoil. And the maximum C_L values at a stall angle of 14° for burst control plates (BCPs) positioned at 0.05c and of width

0.032c and 0.04c are 1.125 and 1.129, which are 21% and 21.42% greater than the maximum value of lift coefficient (0.92978) at stall angle (α) = 10° for clean airfoil. The position that produced the maximum coefficient of lift is found to be at 0.05c for all widths of burst control plate and the width that produced the maximum coefficient of lift is found to be 0.04c at all locations on airfoil. It is because of the reduction in laminar separation bubble (LSB) size and reattachment of the separated flow along the downstream as boundary layer that is separated gets reenergized.

Figures 4.5, 4.7, 4.9, 4.11 and 4.13 show the computed C_D values of BCP width of 0.008c, 0.016c, 0.024c, 0.032c and 0.04c respectively located at 0.045c, 0.05c, 0.07c and 0.1c using Transition SST model, and have been compared to the data of clean airfoil. The results showed that when the angles of attack are less than 8°, all widths burst control plates located at various positions of airfoil have generated more coefficient of drag than airfoil with no BCP. Due to the presence of burst control plate on the upper surface of airfoil toward the leading edge the roughness of surface is increased resulting the addition of skin friction drag. Coefficient of drag has been effectively minimized for all widths BCPs at all locations, when the angles of attack are between 8° and 18°. The coefficient of drag (C_D) for airfoil with burst control plate of width 0.008c at 0.1c position at stall angle (α) = 12° is 0.046 which is lower than the C_D values of other configurations and over 44% less than the C_D value of clean airfoil at stall angle (α) = 10°. But as the angle of attack increases, separation of turbulent boundary layer occurs at the airfoil rear portion which results a gradual increase in coefficient of drag. The values of coefficient of drag (C_D) for all cases are same as C_D of airfoil with no BCP for angle of attack greater than 18°. And the position of BCP that produced the minimum coefficient of drag (C_D) is observed at 0.1c for all widths of burst control plate.

4.4 Effect of plate size located at optimum position on the aerodynamics of airfoil

For all BCP width the maximum lift coefficient is at BCP position 0.05c. Figure 4.14 illustrates the lift coefficients of BCPs width of 0.008c, 0.016c, 0.024c, 0.032c and 0.040c positioned at 0.05c with respect to the airfoil leading edge and compared with clean airfoil at various angles of attack. Results show that for angle of attack less than 8°, C_L is lower than clean airfoil for airfoil with BCPs. When the angle of attack is greater than 8°, the coefficients of lift for all cases are larger than the lift coefficients of airfoil with no BCP. Figure 4.14 also shows that airfoil with BCPs of width 0.008c,

0.016c and 0.024c stall at 12°, and the maximum lift coefficient at 12° is 1.062, shown by BCP of width 0.024c which is 14.22% higher than lift coefficient of clean airfoil at α = 10°. And airfoil with BCPs of width 0.032c and 0.04c stall at 14°, and the maximum lift coefficient at 14° is 1.129, shown by BCP of width 0.04c which is 21.4265% higher than lift coefficient of clean airfoil at α = 10°. The maximum lift coefficient among above configurations is shown by airfoil with BCP width 0.04c at 0.05c at stall angle 14°. At α = 18°, all configurations C_L reattach with C_L of clean airfoil.

Figure 4.15 illustrates coefficients of drag for BCPs of width 0.008c, 0.016c, 0.024c, 0.032c and 0.040c positioned at 0.05c with respect to the airfoil leading edge and compared with clean airfoil at various angles of attack, C_D is greater than clean airfoil for all configurations at angle of attack less than 8°. Among above configurations that have suppressed stall angle by 2°, the minimum drag coefficient is 0.055, shown by airfoil with BCP width 0.008c at 0.05c which is 33.5748% less than drag coefficient of clean airfoil at stall angle. And for the configurations that have suppressed stall angle by 4°, the minimum drag coefficient is 0.08, shown by airfoil with BCP width 0.032c at 0.05c which is 3.38% less than drag coefficient of clean airfoil at stall angle. This might be due to a reduction in the size of LSB. At α = 18°, all configurations C_D reattach with C_D of clean airfoil.

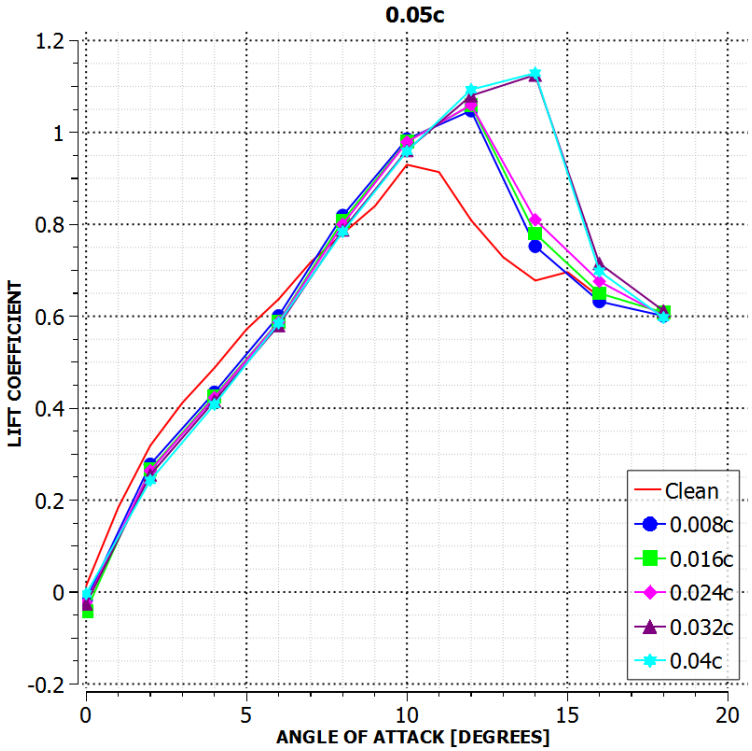

Figure 4.14: Lift coefficient versus angle of attack at the location 0.05c

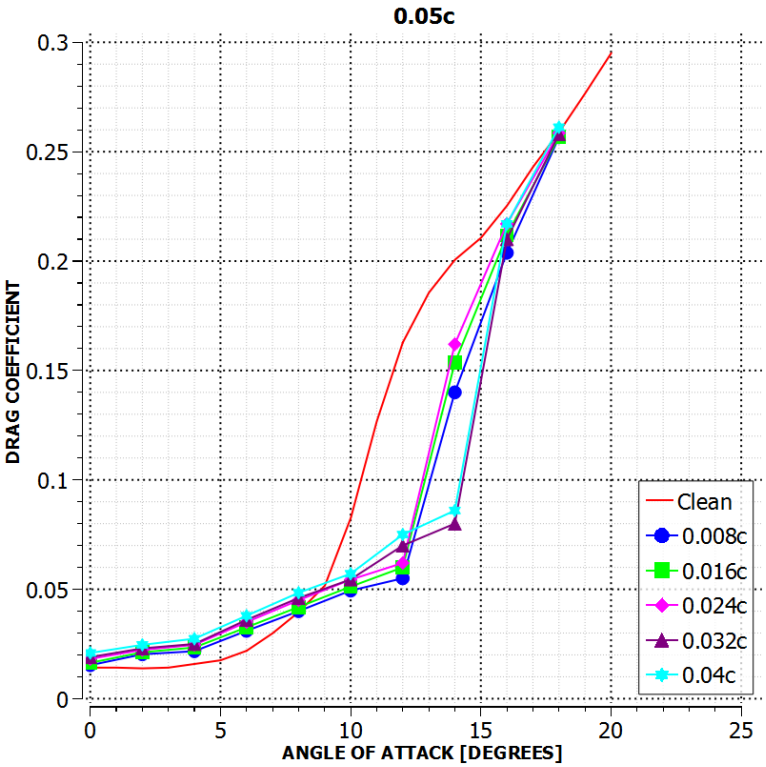

Figure 4.15: Drag coefficient versus angle of attack at the location 0.05c

CHAPTER FIVE: CONCLUSIONS AND RECOMMENDATIONS

5.1 Conclusions

- Rectangular BCPs located at 0.05c from airfoil leading edge are found to be most effective in term of lift coefficient for every width. This may be due to the decrease in size of laminar separation bubble as separated laminar layer transform to turbulent layer and reattach after reenergizing. So, lift coefficient is more than clean airfoil at angle of attack greater than 8°. And BCPs located at 0.1c from leading edge of airfoil generated lowest coefficient of drag for all width in the study. In term of widths, BCP of width 0.04c generated the maximum lift coefficient at every location and BCP of width 0.008c generated the lowest drag coefficient at all positions of study. Stall angle is suppressed from 10° to 14°for BCPs of width 0.032c and 0.04c (greater width) located at 0.045c and 0.05c (nearer to the leading edge of airfoil).
- Among various configurations that have suppressed stall angle from 10° to 14° than the airfoil with no BCPs, the maximum sliding ratio (C_L/C_D) at an angle of attack of 14° is 14.68 which is shown by BCP of width 0.032c positioned at 0.045c with respect to the airfoil leading edge is found to be the best.

5.2 Recommendations

- Few sizes and positions of rectangular burst control plates were studied due to time limitation. Increasing sample of configurations would give more accurate results.
- For this research two-dimensional infinite wing is numerically studied which is unable to capture wing tip vortices resulting error in lift and drag coefficient. Numerical study of three-dimensional finite wing may result more accuracy with finer mesh.
- To study the physics and visualize the flow around the airfoil with burst control plates of various width and location, particle image velocimetry (PIV) system can be used.

REFERENCES

Abbott, L. H. & Von Doenhoff, A. E. (1999). Theory of wind sections New York. Dover Publications Inc.

Anderson, J. D. (2007) Fundamentals of Aerodynamics. New York. The McGraw Hil Companies.

Ashil, P. R. (2000). Studies of flows induced by sub boundary layer vortex generators (SBVGs). 40th ALAA Aerospace and Sciences Meeting and Exhibition Reno NV: AIAA Paper 2002-0968.

Braslow, A. L. (1999). A history of suction type laminar flow control with emphasis on fight research NASA History Division. Monogr. Aerosp. Hist.

CFD Online. (2022, 04 10). Retrieved from http://www.cfd-online.com http://www.cfdc-online.com/Tools/yplus.php.

Choudhry, A., Arjomandi, M., & Kelso, R. (2015). A study of long separation bubble on thick airfoils and its consequent effects. International Journal of Heat and Fluid Flow, 52, 84-96.

Ferziger, J. H., & Peric, M. (1996). Computational methods for fluid dynamics Berlin, Germany: Springer.

Fustui, G. (2010). Experimental study of the behavior of the synthetic jets for effective flow separation control. PhD Thesis.

Gad-el-hak, Pollard, & Bonnet (1998). Flow Control: Fundamentals and Practices Berlin, Heidelberg: Springer-Verlag

Gad-el-hak, M. (2000). Control Flow: Passive, Active and Reactive Flow Management United Kingdom: Cambridge University Press.

Giguere, P. & Selig, M. S. (1997). Low Reynolds number airfoils for small horizontal wind turbines Wind Engineering.

Grager, T. Rothmayer, A., & Hu, H. (2011). Stall Suppression of a Low-Reynolds-Number Airfoil with a Dynamic Burst Control ALAA Paper 2011-1180

Kianoosh, Y., & Reza, S. (2015). Three-dimensional suction flow control and suction jet length optimization of NACA 0012 wing. Meccanica, 1481-1494.

King, P. A., & Breuer, K. S. (2002). Oblique transition in a laminar Blasius boundary layer. Journal of Fluid Mechanics, 453, 177-200.

Kitsios, V., Kotapati, R., Mittal, R., Ooi, A., Soria, J., & You, D. (2006). Numerical simulation of lift enhancement on a NACA 0015 airfoil using ZNMF jets. Proceedings of the Summer Program, (p. 457).

Kurita, S., Rinoie, K., & Sunada, Y. (2008). Stall suppression by use of a rectangular cross-section plate placed on NACA 0012 airfoil. Proc. the 40th Fluid Dynamics Conference, (pp. 331-334). Sendai, Japan.

Lee, S. J., Jeong, E. C., & Lim, H. C. (2013). Numerical study on aerodynamic characteristics of NACA 0015. (J. Wen, Ed.) Applied Mechanics and Materials, 302, pp. 640-645.

Lin, J. C. (1991). Exploratory study of vortex-generating devices for turbulent flow separation control. AIAA 29th Aerospace Sciences Meeting. Reno, NV: AIAA Paper 91-0042.

Lin, J. C. (1999). Control of turbulent boundary layer separation using micro-vortex generators. 30th AIAA Fluid Dynamics Conference. Norfolk, VA: AIAA Paper 99 3404.

Lin, J. C. (2002). Review of research on low-profile vortex generators to control boundary layer separation. Progress in Aerospace Sciences 38, (pp. 389-420).

Lin, J. C., Howard, F. G., Bushnell, D. M., & Selby, G. V. (1990). Investigation of several passive and active methods for turbulent flow separation control. Plasma Dynamics and Lasers Conference. Seattle: AIAA, Fluid Dynamics.

Lissaman, P. B. (1983). Low Reynolds number airfoil. Annual Review Fluid Mechanics, 15, pp. 223-239.

Nakamura, Y., Rinoie, K., & Sunada, Y. (2012). Airfoil Stall Suppression by Use of Rectangular Cross Section Burst Control Plates. In 50th AIAA Aerospace Sciences Meeting including the New Horizons Forum and Aerospace Exposition (p. 318).

Patrick, M. T. (2011). Investigation of a Laminar Airfoil with Flow Control and the Effect of Reynolds Number. The Ohio State University: Department of Aeronautical and Astronautical Engineering.

Richards, E. J., & Burge, C. H. (1943). An airfoil designed to give laminar flow over the surface with boundary layer suction. Aeronautical Research Council. R&M 2263.

Rinioe, K., Okuno, M., & Sunada, Y. (2009). Airfoil Stall Suppression by Use of a Bubble Burst Control Plate. AIAA Journal, 47 (2): 322-330.

Schlichting, H. (1968). Boundary Layer Theory. New York, USA: Mcgraw-Hill.

Shrestha, B. & Bhattarai, N. (2019). Numerical Simulation Studies on Stall Suppression of a NACA 0015 Airfoil. Invention Journal of Research Technology in Engineering and Management.

Sreejith, B. K., & Sathyabhama, A. (2018). Numerical study on effect of boundary layer trips on aerodynamic performance of E216 airfoil. Engineering Science and Technology, 21(1), 77-88.

Wong, C. W., & Rinoie, K. (2009). Bubble burst control for stall suppression on a NACA 63-012 airfoil. 47th AIAA Aerospace Sciences Meeting. AIAA 2009-1111.

APPENDIX A: COORDINATES OF NACA 0012 AIRFOIL

X-coordinate	Y-coordinate		X-coordinate	Y-coordinate
200	0		153.5826	5.8558
199.9506	0.0072		148.1754	6.4336
199.8026	0.0286		145.399	6.722
199.5562	0.0644		142.578	7.0096
199.2114	0.1144		139.7148	7.2956
198.7688	0.1782		136.8124	7.5792
198.2288	0.256		133.8738	7.86
197.5916	0.3474		130.9016	8.1372
196.8584	0.452		127.8992	8.4104
196.0294	0.5698		124.869	8.6788
195.1056	0.7002		121.8144	8.9416
194.088	0.8432		118.7382	9.1984
192.9776	0.998		115.6434	9.4484
191.7754	1.1644		112.5334	9.691
190.4828	1.342		109.4108	9.9252
189.1006	1.5302		106.279	10.1508
187.6306	1.7286		103.141	10.3666
186.0742	1.9368		100	10.5724
184.4328	2.154		96.859	10.767
182.708	2.38		93.721	10.9498
180.9016	2.6142		90.5892	11.1204
179.0156	2.856		87.4666	11.278
177.0514	3.1046		84.3566	11.4216
175.0112	3.36		81.2618	11.551
172.8968	3.6212		78.1856	11.6652
170.7106	3.8876		75.131	11.7638
168.4548	4.159		72.1008	11.846
166.1312	4.4346		69.0984	11.9114
163.7424	4.7138		66.1262	11.9594
161.2908	4.9962		63.1876	11.9894
158.7786	5.281		60.2852	12.0012

X-coordinate	Y-coordinate		X-coordinate	Y-coordinate
54.601	11.9682		0	0
49.0958	11.8576		0.1974	-1.1042
46.4174	11.7726		0.4438	-1.6446
43.7916	11.6676		0.7886	-2.1768
41.2214	11.5424		1.2312	-2.7006
38.7092	11.3972		1.7712	-3.2156
36.2576	11.2318		2.4084	-3.7214
33.8688	11.0464		3.1416	-4.2176
31.5452	10.8412		3.9706	-4.7034
29.2894	10.6166		4.8944	-5.1786
27.1032	10.3724		5.912	-5.6426
24.9888	10.1092		7.0224	-6.0946
22.9486	9.8276		8.2246	-6.5342
20.9844	9.5276		9.5172	-6.9606
19.0984	9.2098		10.8994	-7.3734
17.292	8.8748		12.3694	-7.7718
15.5672	8.523		13.9258	-8.1552
13.9258	8.1552		15.5672	-8.523
12.3694	7.7718		17.292	-8.8748
10.8994	7.3734		19.0984	-9.2098
9.5172	6.9606		20.9844	-9.5276
8.2246	6.5342		22.9486	-9.8276
7.0224	6.0946		24.9888	-10.1092
5.912	5.6426		27.1032	-10.3724
4.8944	5.1786		29.2894	-10.6166
3.9706	4.7034		31.5452	-10.8412
3.1416	4.2176		33.8688	-11.0464
2.4084	3.7214		36.2576	-11.2318
1.7712	3.2156		38.7092	-11.3972
1.2312	2.7006		41.2214	-11.5424
0.7886	2.1768		43.7916	-11.6676
0.4438	1.6446		46.4174	-11.7726

X-coordinate	Y-coordinate		X-coordinate	Y-coordinate
54.601	-11.9682		156.2084	-5.5676
60.2852	-12.0012		158.7786	-5.281
63.1876	-11.9894		161.2908	-4.9962
66.1262	-11.9594		163.7424	-4.7138
69.0984	-11.9114		166.1312	-4.4346
72.1008	-11.846		168.4548	-4.159
75.131	-11.7638		170.7106	-3.8876
78.1856	-11.6652		172.8968	-3.6212
81.2618	-11.551		175.0112	-3.36
84.3566	-11.4216		177.0514	-3.1046
87.4666	-11.278		179.0156	-2.856
90.5892	-11.1204		180.9016	-2.6142
93.721	-10.9498		182.708	-2.38
96.859	-10.767		184.4328	-2.154
100	-10.5724		186.0742	-1.9368
103.141	-10.3666		187.6306	-1.7286
106.279	-10.1508		189.1006	-1.5302
109.4108	-9.9252		190.4828	-1.342
112.5334	-9.691		191.7754	-1.1644
115.6434	-9.4484		192.9776	-0.998
118.7382	-9.1984		194.088	-0.8432
121.8144	-8.9416		195.1056	-0.7002
124.869	-8.6788		196.0294	-0.5698
127.8992	-8.4104		196.8584	-0.452
130.9016	-8.1372		197.5916	-0.3474
133.8738	-7.86		198.2288	-0.256
136.8124	-7.5792		198.7688	-0.1782
139.7148	-7.2956		199.2114	-0.1144
142.578	-7.0096		199.5562	-0.0644
145.399	-6.722		199.8026	-0.0286
148.1754	-6.4336		199.9506	-0.0072
150.9042	-6.1446		200	0

APPENDIX B: Y^+ ESTIMATION TOOL FROM THE CFD ONLINE WEBSITE

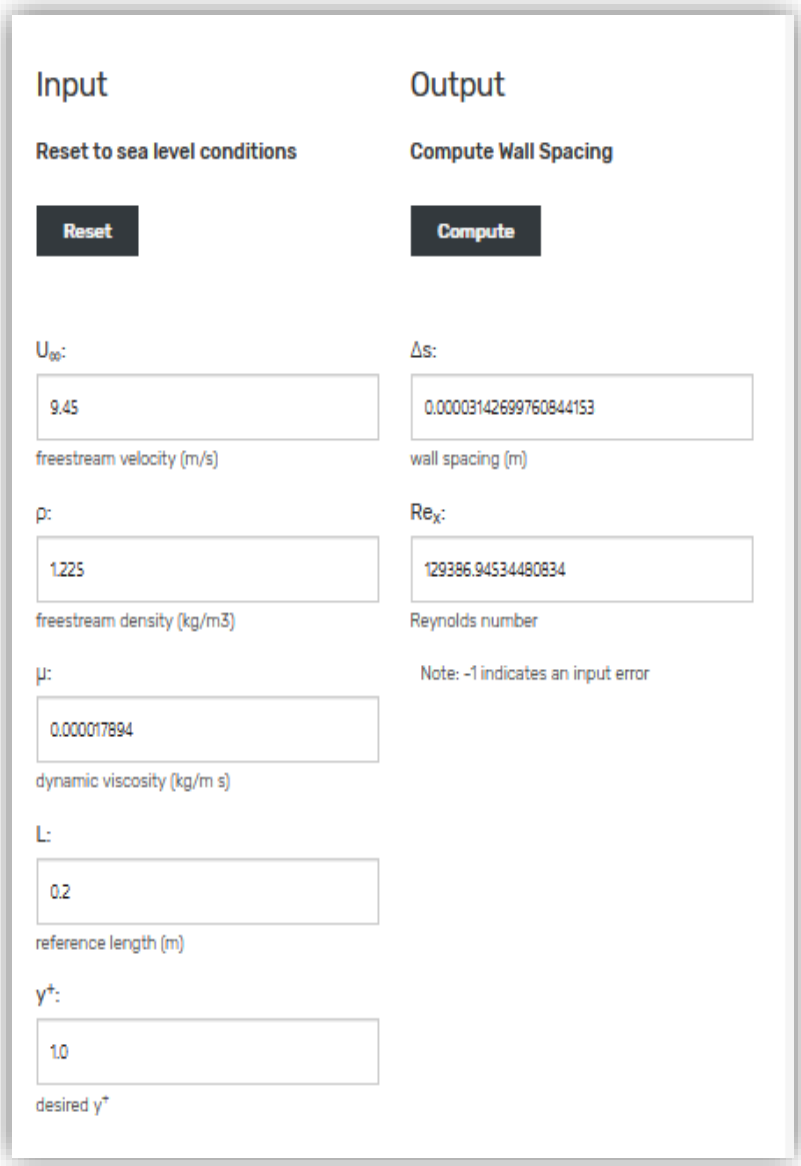

APPENDIX C: COMPUTED C_L, AND C_D, FOR 0.008c WIDTH BCP

	0.045c		**0.05c**		**0.07c**		**0.1c**	
AOA	C_L	C_D	C_L	C_D	C_L	C_D	C_L	C_D
0°	-0.0237	0.0146	-0.0249	0.0153	-0.02276	0.014	-0.02197	0.013
2°	0.289	0.019	0.27769	0.0203	0.305	0.017	0.321	0.016
4°	0.451	0.02	0.43429	0.0217	0.492	0.0191	0.502	0.018
6°	0.62	0.028	0.60061	0.031	0.643	0.026	0.68	0.023
8°	0.84	0.037	0.81912	0.04	0.844	0.035	0.865	0.032
10°	0.984	0.046	0.98543	0.0494	0.9842	0.043	0.983	0.04
12°	1.02	0.052	1.04734	0.055	1.01	0.049	1.004	0.046
14°	0.73	0.117	0.75235	0.14	0.71	0.1045	0.67	0.092
16°	0.61	0.1988	0.63217	0.2038	0.605	0.193	0.601	0.1908
18°	0.6018	0.2565	0.60061	0.2566	0.589	0.2564	0.588	0.2562

APPENDIX D: COMPUTED C_L, AND C_D, FOR 0.016c WIDTH BCP

	0.045c		**0.05c**		**0.07c**		**0.1c**	
AOA	C_L	C_D	C_L	C_D	C_L	C_D	C_L	C_D
0°	-0.0239	0.0157	-0.0252	0.0164	-0.0229	0.0151	-0.022	0.0141
2°	0.28282	0.0199	0.267	0.0212	0.304	0.0179	0.32	0.0169
4°	0.4503	0.0218	0.426	0.0234	0.49	0.0208	0.5	0.0197
6°	0.61275	0.0296	0.588	0.0326	0.642	0.0276	0.675	0.0246
8°	0.82735	0.0399	0.808	0.0419	0.843	0.0369	0.861	0.0339
10°	0.9823	0.0498	0.98	0.0512	0.985	0.0448	0.9857	0.0418
12°	1.04	0.057	1.06	0.06	1.018	0.054	1.008	0.051
14°	0.75	0.1415	0.78	0.1535	0.72	0.123	0.69	0.1105
16°	0.62517	0.2068	0.65	0.2118	0.62	0.201	0.615	0.1988
18°	0.602	0.2566	0.608	0.2567	0.59	0.2565	0.597	0.2563

APPENDIX E: COMPUTED C_L, AND C_D, FOR 0.024c WIDTH BCP

	0.045c		**0.05c**		**0.07c**		**0.1c**	
AOA	C_L	C_D	C_L	C_D	C_L	C_D	C_L	C_D
0°	-0.0241	0.0175	-0.0256	0.0182	-0.0231	0.0169	-0.0221	0.0159
2°	0.27982	0.021	0.264	0.0223	0.3	0.019	0.31	0.018
4°	0.44903	0.023	0.423	0.0246	0.46	0.022	0.49	0.0209
6°	0.60905	0.032	0.587	0.035	0.64	0.03	0.669	0.027
8°	0.82515	0.043	0.8	0.045	0.84	0.04	0.86	0.037
10°	0.9803	0.053	0.979	0.0544	0.9796	0.048	0.974	0.045
12°	1.04665	0.059	1.062	0.062	1.025	0.056	1.011	0.053
14°	0.775	0.15	0.81	0.162	0.76	0.14	0.725	0.119
16°	0.66275	0.212	0.676	0.217	0.64	0.209	0.633	0.204
18°	0.6113	0.2584	0.601	0.2585	0.6	0.2583	0.6101	0.2581

APPENDIX F: COMPUTED C_L, AND C_D, FOR 0.032c WIDTH BCP

	0.045c		**0.05c**		**0.07c**		**0.1c**	
AOA	C_L	C_D	C_L	C_D	C_L	C_D	C_L	C_D
0°	-0.0243	0.018	-0.0258	0.019	-0.0235	0.017	-0.0223	0.0165
2°	0.26782	0.022	0.255	0.023	0.28282	0.021	0.2982	0.019
4°	0.43103	0.024	0.416	0.025	0.441	0.023	0.4603	0.021
6°	0.60575	0.034	0.58	0.036	0.641	0.032	0.67	0.029
8°	0.80115	0.044	0.788	0.046	0.817	0.042	0.84	0.039
10°	0.963	0.054	0.961	0.0545	0.962	0.052	0.967	0.05
12°	1.05977	0.066	1.08	0.07	1.032	0.062	1.023	0.058
14°	1.09425	0.0745	1.125	0.08	0.816	0.15	0.76	0.12
16°	0.69195	0.2	0.715	0.21	0.67	0.21	0.65	0.205
18°	0.626	0.256	0.6118	0.258	0.6002	0.258	0.615	0.257

APPENDIX G: COMPUTED C_L, AND C_D, FOR 0.040c WIDTH BCP

	0.045c		**0.05c**		**0.07c**		**0.1c**	
AOA	C_L	C_D	C_L	C_D	C_L	C_D	C_L	C_D
0°	-0.0247	0.0199	-0.026	0.0209	-0.0236	0.0189	-0.0225	0.0184
2°	0.25982	0.0236	0.243	0.0246	0.273	0.0226	0.297	0.0206
4°	0.42403	0.0264	0.408	0.0274	0.44	0.0254	0.458	0.0234
6°	0.59775	0.0359	0.585	0.0379	0.639	0.0339	0.668	0.0309
8°	0.79145	0.0464	0.784	0.0484	0.81	0.0444	0.837	0.0414
10°	0.9662	0.0563	0.959	0.0571	0.9662	0.053	0.963	0.0529
12°	1.06193	0.07	1.093	0.075	1.09	0.0636	1.06	0.0606
14°	1.09925	0.08	1.129	0.086	0.83	0.16	0.79	0.13
16°	0.69675	0.216	0.698	0.217	0.68	0.22	0.67	0.219
18°	0.602	0.25917	0.597	0.26117	0.61	0.26117	0.607	0.26017

Numerical Analysis on Stall Suppression of a NACA0012 Airfoil

ORIGINALITY REPORT

14%
SIMILARITY INDEX

PRIMARY SOURCES

1	Tohid Moghaddam, Nafiseh Banazadeh Neishabouri. "On the Active and Passive Flow Separation Control Techniques over Airfoils", IOP Conference Series: Materials Science and Engineering, 2017 Crossref	155 words — 1%
2	openscience.fr Internet	117 words — 1%
3	worldwidescience.org Internet	117 words — 1%
4	Biswash Shrestha, Nawraj Bhattarai. "Numerical Simulation Studies on Stall Suppression of a NACA0015 Airfoil", Journal of Advanced College of Engineering and Management, 2021 Crossref	115 words — 1%
5	Chi Wai Wong, Kenichi Rinoie. "Bubble Burst Control Using Smart Structure Sensor Actuators for Stall Suppression", 39th AIAA Fluid Dynamics Conference, 2009 Crossref	99 words — 1%
6	"Flow Control Methods and Their Applicability in Low-Reynolds-Number Centrifugal Compressors—A Review", International Journal of Turbomachinery, Propulsion and Power, 2017	94 words — 1%

Crossref

7	aviationdose.com Internet	76 words — 1%
8	Paweł Ruchała, Robert Placek, Wit Stryczniewicz, Jan Matyszewski, Dawid Cieśliński, Bartosz Bartkowiak. "Wind Tunnel Tests of Influence of Boosters and Fins on Aerodynamic Characteristics of the Experimental Rocket Platform", Transactions on Aerospace Research, 2017 Crossref	73 words — 1%
9	Nvzi Bao, Yehui Peng, Heying Feng, Chenghao Yang. "Multi-objective aerodynamic optimization design of variable camber leading and trailing edge of airfoil", Proceedings of the Institution of Mechanical Engineers, Part C: Journal of Mechanical Engineering Science, 2021 Crossref	68 words — 1%
10	arc.aiaa.org Internet	55 words — < 1%
11	etheses.whiterose.ac.uk Internet	50 words — < 1%
12	Beaugendre, Heloise. "A Pde-Based 3d Approach to In-Flight Ice Accretion.", McGill University (Canada), 2021 ProQuest	47 words — < 1%
13	idr.nitk.ac.in Internet	46 words — < 1%
14	Chi Wai Wong, Satoshi Kurita, Kenichi Rinoie. "Bubble Burst Control for Stall Suppression on a NACA 631-012 Airfoil", 47th AIAA Aerospace Sciences Meeting	45 words — < 1%

including The New Horizons Forum and Aerospace Exposition, 2009
Crossref

15	Lecture Notes in Engineering, 1989. Crossref	37 words — < 1%
16	Rabii El Maani, Soufiane Elouardi, Bouchaib Radi, Abdelkhalak El Hami. "Multiobjective aerodynamic shape optimization of NACA0012 airfoil based mesh morphing", International Journal for Simulation and Multidisciplinary Design Optimization, 2020 Crossref	31 words — < 1%
17	Mohammad H. Sadraey. "Aircraft Design", Wiley, 2012 Crossref	27 words — < 1%
18	Kenichi Rinoie, Takuma Komuro, Yushi Nakamkura, Yasuto Sunada. "Airfoil Stall Suppression Using Rectangular Bubble Burst Control Plate and Sensor Actuators", 6th AIAA Flow Control Conference, 2012 Crossref	25 words — < 1%
19	Kianoosh Yousefi, Reza Saleh. "Three-dimensional suction flow control and suction jet length optimization of NACA 0012 wing", Meccanica, 2015 Crossref	25 words — < 1%
20	Mark Calvert, Tin-chee Wong. "Aerodynamic Impacts of Helicopter Blade Erosion Coatings", 30th AIAA Applied Aerodynamics Conference, 2012 Crossref	25 words — < 1%
21	ndl.ethernet.edu.et Internet	24 words — < 1%

22	Kenichi Rinoie, Masafumi Okuno, Yasuto Sunada. "Airfoil Stall Suppression by Use of a Bubble Burst Control Plate", AIAA Journal, 2009 Crossref	22 words — < 1%
23	Yushi Nakamura, Kenichi Rinoie, Yasuto Sunada. "Airfoil Stall Suppression by Use of Rectangular Cross Section Burst Control Plates", 50th AIAA Aerospace Sciences Meeting including the New Horizons Forum and Aerospace Exposition, 2012 Crossref	22 words — < 1%
24	Kenichi Rinoie, Masafumi Okuno, Yasuto Sunada. "Airfoil Stall Suppression by Use of a Bubble Burst Control Plate", 37th AIAA Fluid Dynamics Conference and Exhibit, 2007 Crossref	21 words — < 1%
25	Ahmed S. Shehata, Qing Xiao, Khalid M. Saqr, Ahmed Naguib, Day Alexander. "Passive flow control for aerodynamic performance enhancement of airfoil with its application in Wells turbine – Under oscillating flow condition", Ocean Engineering, 2017 Crossref	20 words — < 1%
26	repository.ju.edu.et Internet	20 words — < 1%
27	Prasad. G., Ramesh. M., Rajasekar. K.. "Numerical Investigation on Effect of Multiple Winglets for Wind Turbine Applications", International Journal of Engineering & Technology, 2018 Crossref	18 words — < 1%
28	Shields, Allison. "The Development and Application of High-Speed Angiography in Vascular Disease", State University of New York at Buffalo, 2022	18 words — < 1%

ProQuest

29	Sidaard Gunasekaran, Tim Gerham. "Effect of Chordwise Slots on Aerodynamic Efficiency", 2018 AIAA Aerospace Sciences Meeting, 2018 Crossref	18 words — < 1%
30	B.K. Sreejith, A. Sathyabhama. "Numerical study on effect of boundary layer trips on aerodynamic performance of E216 airfoil", Engineering Science and Technology, an International Journal, 2018 Crossref	17 words — < 1%
31	Kok, Cagatay. "Numerical Investigation of Thermal Management for an Airfoil Profile to Prevent Ice Formation.", Izmir Institute of Technology (Turkey), 2021 ProQuest	17 words — < 1%
32	scholarspace.library.gwu.edu Internet	17 words — < 1%
33	Viieru, Dragos. "Flapping and fixed wing aerodynamics of low Reynolds number flight vehicles", Proquest, 20111109 ProQuest	16 words — < 1%
34	archive.org Internet	16 words — < 1%
35	Demetrios Lefas, Jiahuan Cui, Paul G. Tucker. "A Critical Examination of a Correlation-Based Transition Model for Low Pressure Turbines", 55th AIAA Aerospace Sciences Meeting, 2017 Crossref	15 words — < 1%
36	doiserbia.nb.rs Internet	15 words — < 1%

37	a.cii.wwu.edu Internet	14 words — < 1%
38	es.scribd.com Internet	13 words — < 1%
39	Pindado, S.. "Influence of an upstream building on the wind-induced mean suction on the flat roof of a low-rise building", Journal of Wind Engineering & Industrial Aerodynamics, 201108 Crossref	12 words — < 1%
40	citeseerx.ist.psu.edu Internet	12 words — < 1%
41	link.springer.com Internet	12 words — < 1%
42	www.coursehero.com Internet	12 words — < 1%
43	Pereira, Bernardo Correia. "Numerical Analysis of Flow Around a Fan Blade of a CFM56-3", Universidade da Beira Interior (Portugal), 2021 ProQuest	11 words — < 1%
44	MITTAL, S.. "CONTROL OF FLOW PAST BLUFF BODIES USING ROTATING CONTROL CYLINDERS", Journal of Fluids and Structures, 200102 Crossref	10 words — < 1%
45	"Applications of Circulation Control Technology", American Institute of Aeronautics and Astronautics (AIAA), 2006 Crossref	9 words — < 1%